Lithos 372–373 (2020) 105665

Contents lists available at ScienceDirect

Lithos

journal homepage: www.elsevier.com/locate/lithos

Research Article

Hf-O isotope systematics of zircons from the Taitao granitoids: Implications for slab-melting material

Kazue Suzuki [a], Yusuke Sawaki [a,*], Tsuyoshi Iizuka [b], Kouki Kitajima [c], Kentaro Hattori [d], Takafumi Hirata [d], Ryo Anma [e]

[a] Department of Earth Science and Astronomy, Graduate School of Arts and Sciences, The University of Tokyo, 3-8-1 Komaba, Meguro-ku, Tokyo, Japan
[b] Department of Earth and Planetary Sciences, The University of Tokyo, 7-3-1, Hongo, Bunkyo-ku, Tokyo, Japan
[c] WiscSIMS, Department of Geoscience, University of Wisconsin, 1215, W. Dayton St., Madison, WI 53706, USA
[d] Geochemical Research Center, Graduate School of Science, The University of Tokyo, 7-3-1, Hongo, Bunkyo-ku, Tokyo, Japan
[e] Graduate School of Technology, Industrial and Social Sciences, Tokushima University, 2-24, Shinkura-cho, Tokushima 770-8501, Japan

ARTICLE INFO

Article history:
Received 31 March 2020
Received in revised form 25 June 2020
Accepted 25 June 2020
Available online 04 July 2020

Keywords:
Slab-melting
Ridge-subduction
Oxygen isotope
Hafnium isotope
Taitao granitoids

ABSTRACT

Slab-melting is considered to have played an important role in the formation of continental crust. The combination of oxygen (O) and hafnium (Hf) isotope signatures can provide key information relating to the melting components during slab-melting. To reveal the melting components, we used SIMS and LA-ICP-MS to determine O isotope ratios at 220 spots and Hf isotope ratios at 61 spots in zircons from five plutons in the Taitao Peninsula, where slab-melting occurred at ca. 4–5 Ma. In addition, we measured whole-rock Hf—O isotope ratios in 11 rocks that were intruded by the granitoids. The zircon $\delta^{18}O$ values of the Seno Hoppner pluton (5.37 ± 0.44‰) are identical to those of mantle-equilibrated zircons, whereas those of the other four plutons are relatively high (6.09–6.53‰). The εHf(t) values of zircons in the granitoids are negatively correlated with $\delta^{18}O$, and they fell along the mixing line between a juvenile component and sedimentary rocks. Therefore, the Hf—O profiles can be attributed to mixing of juvenile granitoid magma and the sedimentary rocks, the amount of which was likely minimal in the Seno Hoppner pluton. As such, the $\delta^{18}O$ values of the Seno Hoppner pluton could best reflect the juvenile component. In view of the $\delta^{18}O$ variation in whole-rock samples of the Taitao ophiolite, the melting of hydrothermally altered basalt and dolerite is considered responsible for the juvenile magma generation. This further implies that juvenile granitoid magmas can be generated by the melting of the upper half of subducted oceanic crusts.

© 2020 Elsevier B.V. All rights reserved.

1. Introduction

Revealing generation process of granitoid magma is critical to understanding the mechanism of continental crust formation. Melting of subducting crust— slab-melting—is an important model for the formation of granitoid. This process was first proposed with robust foundations in the Adak Island in Aleutians by Kay (1978). Slab-melting is suggested to have mainly occurred in the Archean owing to the high temperature of subducting oceanic crust at that time (e.g., Martin, 1986, 1999), but subduction of hot oceanic crust has occurred locally even at present (Defant and Drummond, 1990; Iwamori, 2000; Nelson and Forsythe, 1989). For example, it is suggested that post-Oligocene adakite was formed during slab-melting, because the rock mainly exists at localities where young (< 25 M.y.) and hot oceanic crust is subducting (Defant and Drummond, 1990). In addition, in the absence of high rates of shear heating, fluid-absent partial melting of subducting oceanic crust would occur during subduction of slab younger than 2–5 M.y. (Peacock et al., 1994). As another example, it is suggested that the Cretaceous granitoids in southwestern Japan were also formed by Kula–Pacific ridge subduction (e.g., Kinoshita, 1999; Uyeda and Miyashiro, 1974). Although various models have been proposed for the magma production during subduction of slab (e.g., Kay and Kay, 2002), it is considered that slab-melting may have played an important role in granitoid formation in the post-Archean.

The detailed mechanisms of slab-melting are not completely understood; in particular, it is still uncertain which part of the slab is melted. The upper part of the slab is composed of gabbro, doleritic dike, basaltic lava, and overlying sediments. Because these components have different oxygen (O) isotope ratios (e.g., Gregory and Taylor, 1981; Kempton et al., 1991; Lécuyer and Gruau, 1996), O isotopic data for whole rocks and minerals have often been used to constrain the nature of the protolith that was melted to form igneous rock (e.g., Lackey et al., 2008; Matsuhisa, 1979). Previous works have reported the O isotope ratios ($\delta^{18}O$) of adakite lavas, which possibly contain melt from subducted oceanic crust, to identify their source rocks in the Andean Austral

* Corresponding author.
E-mail address: y-sawaki@g.ecc.u-tokyo.ac.jp (Y. Sawaki).

https://doi.org/10.1016/j.lithos.2020.105665
0024-4937/© 2020 Elsevier B.V. All rights reserved.

Volcanic Zone (Stern and Kilian, 1996), the Western and Central Aleutians, the Andes, Panama, Fiji, Kamchatka, Setouchi, and the Cascades (Bindeman et al., 2005). The combination of $\delta^{18}O$ value, trace element composition, and other isotopic signatures in these lavas implies that the $\delta^{18}O$ value of end-member adakitic melt without involvement of sediment melt is identical to, or slightly higher than, that of mantle peridotite ($\delta^{18}O = 5.5 \pm 0.2‰$) (Eiler, 2001; Mattey et al., 1994). Bindeman et al. (2005) proposed three possible mechanisms to account for the $\delta^{18}O$ value: (i) whole melting of the subducting oceanic crust, (ii) interaction of slab melt with mantle peridotite during magma ascent, and (iii) partial melting of mafic lower crust that was transported deeper by delamination or subduction–erosion. Because a possibility remains that the adakite magmas interacted with mantle during ascent, the adakites may not reflect the $\delta^{18}O$ value of the initial melt itself from subducted oceanic crust.

To circumvent this problem, we focused on the Taitao granitoids in western Chile (Fig. 1). It has been suggested that these granitoids were formed by slab-melting owing to ~5 Ma spreading ridge subduction (e.g., Anma et al., 2009), and a seismic study suggested that there is no mantle wedge in western Chile (Behrmann et al., 1994). Therefore, it is expected that the $\delta^{18}O$ values of the Taitao granitoids more directly reflect those of the initial magma generated by slab-melting. Moreover, at the Taitao peninsula, the candidates for the protolith of the Taitao granitoids crop out well as the Taitao ophiolite, a fragment of the subducted spreading ridge (Bourgois et al., 2016; Forsythe and Nelson, 1985; Nelson et al., 1993). Accordingly, an O isotopic study of the Taitao granitoids and ophiolite potentially provides new insights into the melted portion within the oceanic crust.

One major challenge in estimating the O isotope composition of initial slab melt for the Taitao granitoids is assessing the contamination of melts by sediments. The Taitao granitoids intruded into the sedimentary rocks of the pre-Jurassic basement. The strontium (Sr) isotope ratios of the granitoids indicate contamination by the sediments during its formation (Kaeding et al., 1990; Shin et al., 2015). Because clastic sediments and pelagic clays commonly have high $\delta^{18}O$ values (10–20‰ and 15–25‰, respectively; Eiler, 2001), the $\delta^{18}O$ value of primary granitoid magma should change owing to the involvement of these sediments.

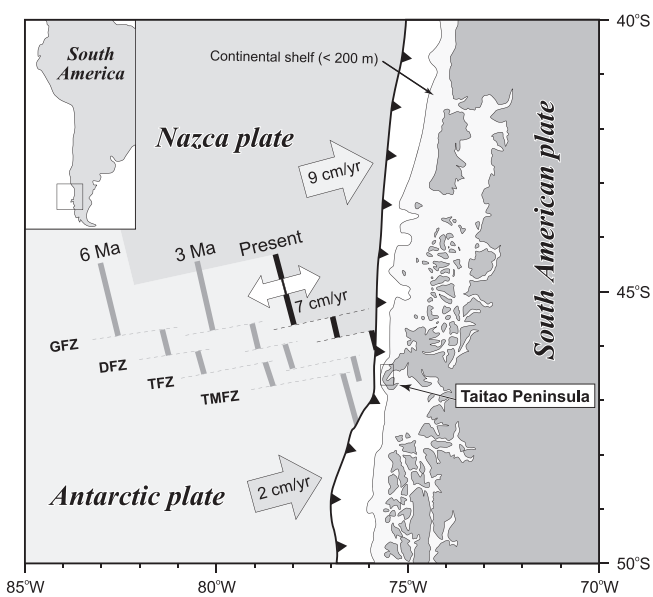

Fig. 1. Tectonic map of the southwestern margin of South America (modified after Kon et al., 2013). The spreading center of the Chile ridge system between the Nazca and Antarctic plates subducts beneath the South American plate. The locations of the Chile ridge system at present, 3 Ma, and 6 Ma are shown in black and gray bars. The convergent rates of the Nazca plate and Antarctic plate are 9 cm/yr and 2 cm/yr, respectively. DFZ: Darwin fracture zone, GFZ: Guamblin fracture zone, TFZ: Taitao fracture zone, TMFZ: Tres Montes fracture zone.

The O isotope ratios of non-metamict zircons ($\delta^{18}O_{Zrc}$) reflect the $\delta^{18}O$ value of the protolith rather than the whole-rock $\delta^{18}O$ ($\delta^{18}O_{WR}$) values, because the $\delta^{18}O_{WR}$ value is usually modified by subsolidus processes (e.g., Eiler, 2001; Eiler et al., 2000; Ito et al., 2003; Lackey et al., 2008; Matsuhisa, 1979; Taylor Jr and Sheppard, 1986). On the other hand, the $\delta^{18}O_{Zrc}$ value is highly resistant to post-crystallization modification and nearly constant irrespective of SiO_2 content (Cherniak and Watson, 2003; Lackey et al., 2008; Valley et al., 1994). Hafnium (Hf) isotopic compositions of zircon can also be used to evaluate the degree of sediment contamination (e.g., Kemp et al., 2007), because clastic sediments generally have distinct Hf isotopic compositions (low $^{176}Hf/^{177}Hf$ ratios). Therefore, we performed in situ O and Hf isotope analyses on zircons from the Taitao granitoids. In addition, in order to constrain the source rocks of the granitoids, we measured whole-rock O—Hf isotope ratios of rocks in the Taitao ophiolite and the pre-Jurassic basement. The combination of Hf and O systematics enabled us to constrain the protoliths of the Taitao granitoids, which provided further information relating to the dominant melting component within subducted oceanic crust.

2. Geology

2.1. Geological setting of the Taitao granitoid

The westernmost part of the Taitao peninsula is composed of pre-Jurassic meta-sedimentary rocks (the Los Chonos complex), the Taitao ophiolite, and the Taitao granitoids. The Taitao granitoids are exposed ~50 km southeast of the Chile triple junction, where the spreading center of the Chile ridge between the Nazca plate and Antarctic plate is subducting beneath the South American plate (Fig. 1). Geophysical studies have indicated that spreading centers subducted repeatedly almost at the same location (the offshore area of the Taitao peninsula) at around 6 Ma, 3 Ma, and at present (Cande and Leslie, 1986; Forsythe et al., 1986; Guivel et al., 1999). On the basis of spatial and temporal correlations between the granitoids and subducted ridges, the Taitao granitoids are considered to be formed as a result of the ridge subduction (Forsythe et al., 1986). The Taitao granitoids are distributed around the Taitao ophiolite and include four main bodies and an intrusion: the Estero Cono, the Seno Hoppner, the Cabo Raper, and the Tres Montes plutons and a small intrusive body in the Bahia Barrientos (Fig. 2). The compositions of these granitoids range from tonalite, through trondhjemite and granodiorite, to granite (e.g., Kon et al., 2013). Crystallization ages of the Tres Montes pluton (5.70 ± 0.25 Ma), the Seno Hoppner pluton (5.17–5.09 ± 0.09 Ma), the Estero Cono pluton (5.12 ± 0.09 Ma), the Bahia Barrientos intrusion (4.88 ± 0.07 Ma), and the Cabo Raper pluton (3.84–3.97 Ma) were determined by SHRIMP U—Pb dating of zircon (Anma et al., 2009; Hervé et al., 2003). Zircon fission track dating for the Estero Cono pluton and Bahia Barrientos intrusion yielded ages of 3.49 Ma and 3.47 Ma, respectively (Hervé et al., 2003). It is widely accepted that rare earth element (REE) abundances in granitoids are useful for investigating the depth of granitoid magma genesis (Defant and Drummond, 1990; Martin, 1986). As such, the heavy rare earth element (HREE)-depleted composition ($4 < Yb_N < 9$) and moderately fractionated REE pattern ($[La/Yb]_N \leq 10$) in the Cabo Raper pluton, together with its isotopic signatures ($I_{Sr} \sim 0.7045$, $\varepsilon_{Nd} \sim +1.5$), have been used to argue for magma generation by partial melting of garnet-bearing altered mafic igneous rocks (Bourgois et al., 1996). However, their Sr contents and $[La/Yb]_N$ values are lower than those of typical HREE-depleted Archean Tonalite–Trondhjemite–Granodiorite (TTG), which are also considered to be generated in the garnet stability field. Furthermore, granitoids from the Cabo Raper, Estero Cono, and Seno Hoppner plutons show high Y (10–50 ppm) and Yb contents ($8 < Yb_N < 35$), low Sr/Y ratios ($1 < Sr/Y < 20$), and moderately low La/Yb ratios ($5 < [La/Yb]_N < 20$)

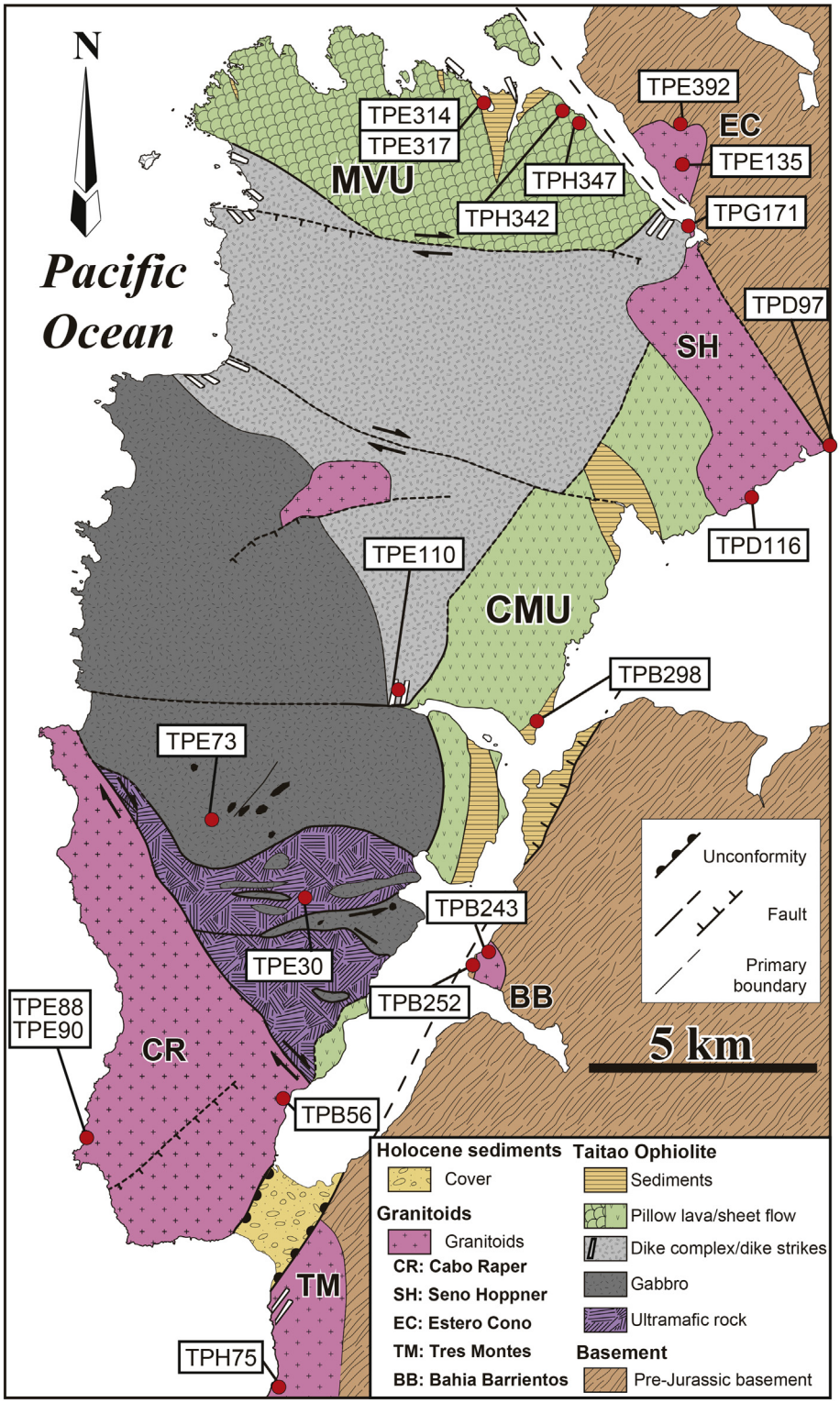

Fig. 2. Geological map of the Taitao Peninsula (modified after Anma et al., 2006). CR: Cabo Raper pluton, EC: Estero Cono pluton, SH: Seno Hoppner pluton, TM: Tres Montes pluton, BB: Bahia Barrientos intrusion, MVU: Main Volcanic Unit, CMU: Chile Margin Unit.

(Kon et al., 2013). These chemical compositions are more similar to those of post-Archean granitoids and island arc Andesite–Dacite–Rhyolite (ADR) rather than those of Archean TTG and adakite. This suggests that the granitic magma was generated by partial melting within the stability field of plagioclase rather than garnet. In view of their compositions together with depth of subducting oceanic crust near the Chile triple junction (Bangs et al., 1992; Cahill and Isacks, 1992; Couch et al., 1981), Kon et al. (2013) concluded that the granitoid magma was generated by slab-melting at <30 km depth.

Based on radiogenic Sr and non-radiogenic Nd isotope ratios ($^{87}Sr/^{86}Sr$ = 0.70435–0.70497, $^{143}Nd/^{144}Nd$ = 0.51271–0.51288), Kaeding et al. (1990) suggested that the Cabo Raper pluton, Bahia

Barrientos intrusion, and Seno Hoppner pluton involved ~15%, ~15%, and ~ 10% sediments, respectively, during either magma generation or ascent. Shin et al. (2015) also suggested 5–10% incorporation of sedimentary rocks into the Seno Hoppner pluton. Based on Sr and Nd isotopic data from the Taitao granitoids ($^{87}Sr/^{86}Sr$ = 0.70408–0.70818, $^{143}Nd/^{144}Nd$ = 0.51244–0.51283), the Taitao ophiolite, and the basement rocks, these workers further indicated that more abundant sedimentary rocks were involved in the Cabo Raper, Estero Cono, and Tres Montes plutons and the Bahia Barrientos intrusion as compared with the Seno Hoppner pluton.

We analyzed Hf—O isotope ratios and chemical compositions in zircons separated from three tonalites from the Cabo Raper pluton, two trondhjemites from the Seno Hoppner pluton, one tonalite from the Estero Cono pluton, one tonalite from the Bahia Barrientos intrusion, and one granite from the Tres Montes pluton (Table S1). Sampling localities are shown in Fig. 2.

2.2. Geological setting of the Taitao ophiolite

The Taitao ophiolite consists of sedimentary rocks, pillow lava/sheet flows, rhyolites, sheeted doleritic dikes, gabbros, and ultramafic rocks (Fig. 2; Forsythe et al., 1986; Nelson et al., 1993; Bourgois et al., 1993, 2016; Guivel et al., 1999; Veloso et al., 2005; Anma et al., 2006; Shibuya et al., 2007). The ophiolite contains a complete sequence of oceanic crust, but the internal structure of the ophiolite is complex because of many thrusts and folds (Veloso et al., 2005). Volcanic sequences (pillow lava/sheet flows) are separated into two bodies: the main volcanic unit (MVU) in the northern region and the Chile margin unit (CMU) in the eastern region of the ophiolite. The sheeted dikes, gabbros, and ultramafic rocks are partially intruded by the Taitao granitoids. Based on the metamorphic zone boundaries subparallel to the internal lithologic boundaries, it is considered that the Taitao ophiolite suffered seafloor hydrothermal metamorphism at a mid-ocean ridge (Shibuya et al., 2007).

Whole-rock K—Ar ages from the MVU and CMU range from 4.6 Ma to 2.5 Ma (Mpodozis et al., 1985). Anma and Orihashi (2013) recently reported zircon U—Pb ages of the CMU ranging from 5.2 Ma at the Southern Taitao Ridge off-shore the Taitao peninsula to 4.9 Ma in the northern part. Anma et al. (2006) presented zircon SHRIMP U—Pb ages of 5.66–5.59 Ma for the gabbros and 5.19 Ma for the sheeted dikes. Based on these ages, they concluded that ridge subduction took place since 6 Ma.

In this study, we selected samples for whole-rock Hf—O analyses (based on metamorphic temperatures calculated by Shibuya et al. (2007) to cover the entire section of oceanic crust (Table S1). We selected two lavas in the MVU (TPH342 and TPH347), and their metamorphic temperatures were estimated to be ca. 200 °C and ca. 200–350 °C, respectively. We further selected a dolerite (TPE110) whose metamorphic temperature was estimated to be 347–375 °C. A gabbro (TPE73) and a pyroxenite (TPE30) were selected, because they were located close to the metamorphic temperature-constrained gabbro (TPE72; 550 °C) and peridotite (TPE014; 750–850 °C). Four sedimentary rocks in the MVU and two sedimentary rocks in the pre-Jurassic basement rocks were chosen to cover the variations in rock type.

2.3. Petrography of the Taitao granitoids

Representative photographs of rock specimens and thin sections of the granitoids are shown in Fig. 3. The granitoids displayed equigranular textures and mainly consisted of plagioclase, quartz, biotite, K-feldspar, and hornblende with minor amounts of muscovite (Figs. 3B, C, and D), and modal abundance in each sample is summarized in Table S1. Chlorite and actinolite were observed as secondary minerals, and accessory minerals were magnetite, ilmenite, zircon, and apatite. Samples TPE90, TPE88, and TPB56 from the Cabo Raper pluton, TPD116 from the Seno Hoppner pluton, TPE135 from the Estero Cono pluton, and TPB243 from the Bahia Barrientos intrusion were composed of medium- to coarse-grained minerals, and their average lengths were ca. 1 mm (e.g., Fig. 3C). Sample TPG171, a microtrondhjemite dike which intruded into hornfels of the Seno Hoppner pluton, is composed of relatively fine-grained minerals with average lengths of ca. 400 μm (Figs. 3A and B). The sample contained aggregates of fine-grained hornblende and plagioclase (~10–200 μm, Fig. 3B). Sample TPH75 was collected from a leucocratic granitic dike which was formed during the intrusion of *syn*-plutonic melanocratic dike into the Tres Montes pluton. The granite is composed of medium-grained minerals (~1 mm) with fine-grained quartz that exhibits a mosaic texture (Fig. 3D).

A normative An–Ab–Or diagram (after Barker, 1979) for selected granitoids is shown in Fig. 4 (analytical methods and whole-rock compositions of the granitoids are given in the supplementary file). As seen in previous studies (e.g., Anma et al., 2009; Kon et al., 2013), samples from the Bahia Barrientos intrusion and Cabo Raper and Estero Cono plutons plotted within the tonalite field. Samples from the Seno Hoppner pluton plotted within the trondhjemite field (Fig. 4). The composition of TPD116 coincided with samples from the Seno Hoppner pluton, as reported in previous studies (e.g., Anma et al., 2009; Kon et al., 2013). On the other hand, sample TPG171 is K-poor, and its chemical composition is different from that of any other Taitao granitoids. Sample TPH75 from the Tres Montes pluton is plotted on the boundary between the granite and quartz monzonite fields; it also had a composition distinct from other granitoids (Fig. 4).

2.4. Petrography of the rocks in the Taitao ophiolite and pre-Jurassic basement

Representative photographs of thin sections of the nine samples from the Taitao Ophiolite and two samples from pre-Jurassic basement rocks are shown in Fig. 3. The lavas in the MVU (TPH342 and TPH347) are composed of fine-grained plagioclase, clinopyroxene, quartz, and glass, and they include chlorite, epidote, prehnite, and laumontite as alteration minerals (Shibuya et al., 2007; Fig. 3E). Almost all plagioclase grains in the lavas showed a hollow crystal structure. The dolerite (TPE110) shows an aphyric texture composed of fine-grained minerals, and igneous clinopyroxene still partly remains (Fig. 3F). As alteration minerals, chlorite, plagioclase, epidote, actinolite, hornblende, and carbonate are included (Shibuya et al., 2007). The gabbro (TPE73) is composed of coarse-grained olivine, orthopyroxene, clinopyroxene, plagioclase and subordinate amounts of magnetite and ilmenite (Fig. 3G). The coarse-grained pyroxenite (TPE30) is composed of clinopyroxene, olivine, plagioclase, magnetite, and picotite. Serpentine and chlorite were observed as alteration minerals in the gabbro and pyroxenite. The existence of hydrous minerals in the lavas, dolerite, gabbro, and pyroxenite suggests that these samples underwent hydrothermal alteration.

A representative photograph of the sedimentary rocks from the pre-Jurassic basements (TPB252) is shown in Fig. 3H. The sedimentary rocks mainly consist of quartz, feldspar, muscovite, and biotite of visible (> 20 μm) sizes. The mosaic texture observed in TPH75 from the Tres Montes pluton is similar to the texture of TPB252 (Fig. 3D and H).

3. Sample preparation and analytical procedures

Detailed analytical procedures for whole-rock major element composition analysis, zircon U—Pb dating, and REE concentrations in zircon are provided in the supplementary file and Table S2. In the following paragraphs, we introduce analytical methods for O and Hf isotope ratio measurements.

3.1. Zircon separation and observation techniques

Zircon grains were extracted from three tonalites of the Cabo Raper pluton, two trondhjemites of the Seno Hoppner pluton, one tonalite of

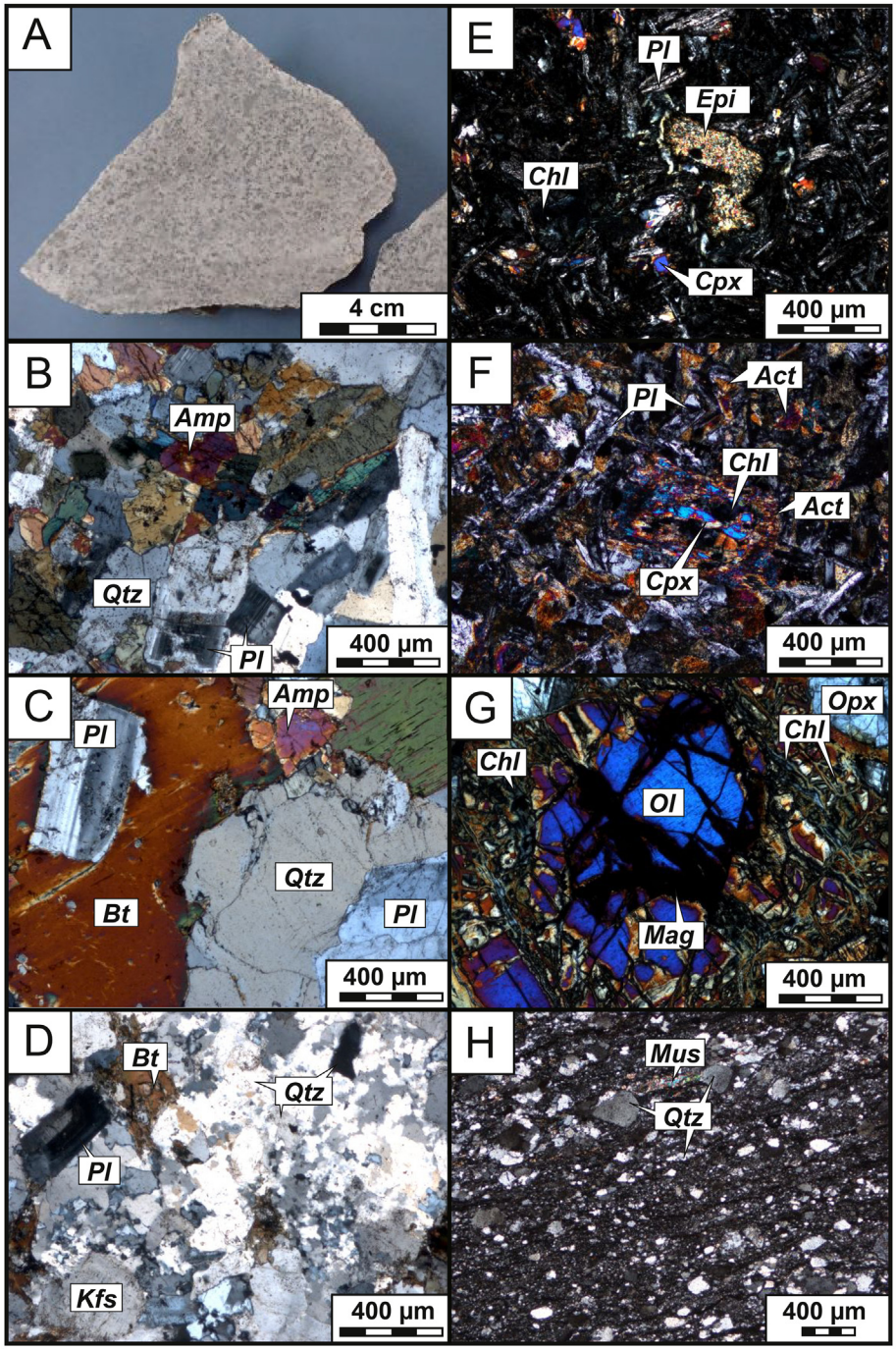

Fig. 3. (A) Representative photograph of microtrondhjemite (TPG171) in the Seno Hoppner pluton. (B–D) Representative microscopic photographs of the Taitao granitoids: microtrondhjemite (TPG171) in the Seno Hoppner pluton (B), tonalite (TPE90) in the Cabo Raper pluton (C), and granite (TPH75) in the Tres Montes pluton (D). (E–H) Representative microscopic photographs of rocks constituting the Taitao ophiolite and basement: basaltic lava (TPH342) in the MVU (E), dolerite (TPE110) in the ophiolite (F), gabbro (TPE73) in the ophiolite (G), and mudstone (TPB252) in the basement (H).

the Estero Cono pluton, one tonalite of the Bahia Barrientos intrusion, and one granite of the Tres Montes pluton by standard crushing, panning, and magnetic separation techniques. The grains were mounted in 25-mm epoxy disks with chips of KIM-5 standard zircon (Valley, 2003; Valley et al., 1998) and polished until the midsections of the grains were exposed. The internal structures of the zircons and the presence of inclusions were assessed using transmitted and reflected light optical microscopy and cathodoluminescence (CL) imaging. The CL images were acquired using a Hitachi S-3400 N scanning electron microscope (Hitachi High Tech. Corp., Japan) with a Chroma CL2 sensor (Gatan, Inc., USA) at the Tokyo Institute of Technology. Before in situ analyses, we described the internal textures of the zircons as rim, magmatic core, and inherited core, and selected the analytical spots. We conducted U—Pb dating (Table 1), trace element analysis (Table S3), and O and Hf isotope analyses (Tables 2 and 3) on the zircons.

3.2. In situ O isotope analysis

Before O isotope analysis, the epoxy mounts were washed with deionized water and ethanol in an ultrasonic bath. The mounts were

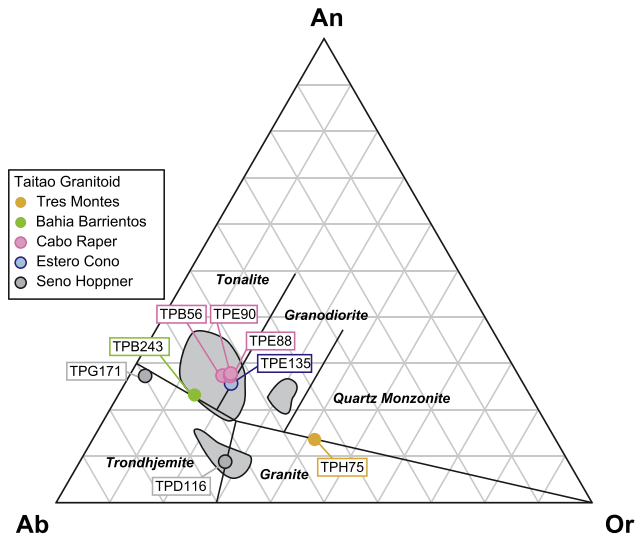

Fig. 4. Normative An–Ab–Or diagram (after Barker (1979)). Gray areas indicate compositions of the Taitao granitoids, as reported by Kaeding et al. (1990); Bourgois et al. (1996); Guivel et al. (1999); Anma et al. (2009); Kon et al. (2013); and Shin et al. (2015).

dried in N_2 gas and a vacuum oven prior to coating with Au for SIMS O isotope analysis. The O isotope ratios were determined using a CAMECA IMS-1280 at the WiscSIMS Laboratory in the University of Wisconsin–Madison, following the procedures reported by Kita et al. (2009) and Valley and Kita (2009). In situ O isotopes were analyzed using a 2.0–2.2 nA primary Cs^+ beam with a ~ 10 μm spot size. Secondary ^{16}O and ^{18}O ions were measured simultaneously using two Faraday cup detectors. KIM-5 zircon ($\delta^{18}O = 5.09‰$ relative to Vienna standard mean ocean water (VSMOW); Valley, 2003) was used as a standard, and the average value of eight standard analyses bracketing each 10 analyses of unknowns was used to correct for instrumental bias. The precision of each analysis (ca. 0.3‰ on average) was estimated based on 2 standard deviations (SD) of the reproducibility of the bracketing standard analyses. The O isotope ratios are reported using standard per mil notation ($\delta^{18}O_{Zrc}$) relative to VSMOW (Table 2). During the O isotope analysis, we monitored $^{16}OH/^{16}O$ values for each zircon standards and samples to evaluate influence of metamict. The $^{16}OH/^{16}O$ values in the samples are very low as well as KIM-5 (Table S4).

3.3. In situ Hf isotope analysis

We measured Hf isotope ratios at the same spots used for the O isotope analysis (Fig. 5) using a LSX-213 G2+ laser ablation system (Teledyne CETAC) coupled with a Neptune Plus multicollector inductively coupled plasma mass spectrometer (MC-ICP-MS; Thermo Fisher Scientific) at the University of Tokyo. Data were acquired from ~40 μm ablation pits with a laser repetition rate of 4 Hz and ~ 60 s ablation times. He gas was used as a carrier gas to promote sample transport efficiency and minimize the redeposition of sample aerosol around the ablation pit. Furthermore, ~5 mL/min N_2 was mixed into the carrier gas to enhance signal intensity (Iizuka and Hirata, 2005). Instrumental mass bias and isobaric interferences of Yb and Lu on Hf were corrected following the data reduction protocols of Iizuka and Hirata (2005). Mud Tank zircon was chosen for normalization of the isotope ratios. The analytical errors combine the internal run errors (2 standard errors [SE]) and the reproducibility of the Mud Tank standard zircon analyses (2 SD), added in quadrature. To evaluate the accuracy and precision of our data acquisition, we performed repeated analyses of the zircon standards R33 and FC-1. Data obtained during the course of this study yielded mean initial $^{176}Hf/^{177}Hf$ of 0.282742 ± 69 (2 SD, $n = 28$) for R33. These results are in good agreement with the initial $^{176}Hf/^{177}Hf$ ratios determined by wet analysis using MC-ICP-MS (0.282767 ± 18 for R33; Fisher et al., 2014). More detailed analytical procedures are given by Iizuka et al. (2013). Hf isotopic value of zircon is reported as εHf (t) based on its $^{238}U—^{206}Pb$ age.

3.4. Whole-rock O isotope analysis

Powdered 11 samples prepared from ophiolite body, sediments, basement rocks (Table S1), and standard powders (2–3 mg) were loaded into individual nickel pins. The loaded pins were placed in a sample tray within an airlock chamber and evacuated for 2–3 h (to $<10^{-3}$ Torr). Samples and standards were then individually transferred for each analysis through a gate valve to an evacuated analysis chamber for laser fluorination. After the gate valve was closed (isolating unreacted samples in the airlock chamber), BrF_5 was introduced into a U-shaped trap immersed in liquid nitrogen (−196 °C), and then both the U-shaped trap and the analysis chamber were again evacuated. The analysis chamber was isolated from the vacuum line, and the BrF_5 was liberated by heating the U-shaped trap. The remaining steps, including laser heating, sample gas purification, conversion to CO_2, and O isotopic measurement, were identical to standard laser fluorination procedures (Spicuzza et al., 1998; Valley et al., 1995). O isotopic measurement was performed on a triple-collecting Finnigan/MAT 251 mass spectrometer (Thermo Fisher Scientific) at the University of Wisconsin–Madison.

3.5. Whole-rock Hf isotope analysis

The 11 rocks collected from the ophiolite body, sediments, and basement rocks were prepared for whole-rock Hf isotope measurement (Table S1). Thin (~1 cm thick) rock chips weighing about 20–70 g were cut from fresh samples. The chips were washed with distilled water using an ultrasonic device, dried completely at 120 °C, and then crushed using a stainless mortar, an agate ball mill, and an agate mortar. Next, 20–200 mg samples of the powders were decomposed with concentrated HF + HNO_3 in sealed Teflon beakers at ~200 °C. The decomposed samples were converted to a soluble form by repeated evaporation with concentrated HNO_3 + $HClO_4$, followed by re-dissolution in 6 N HCl at 120 °C. Chemical separation of Hf was performed by a two-step ion exchange procedure. In the first separation step, 0.05 mL of Bio-Rad anion exchange resin (AG1-X8; 200–400 mesh) was loaded into the column. As such, matrix elements were removed, and Hf was recovered with 6 N HCl. Hf was further purified in the second step using 0.1 mL of Eichrom Ln-spec resin (100–150 μm); the Hf was recovered with 0.5 N HNO_3 and 0.2 N HF. The purified Hf fractions were evaporated and dissolved in 2 mL of 0.5 N HNO_3 with a trace amount of HF for isotope analysis. Procedural Hf blanks were 2–6 pg.

The Hf isotopic measurements were performed on a Neptune Plus MC-ICP-MS attached to an Aridus II desolvating nebulizer (CETAC Technologies) at the University of Tokyo. The instrument was equipped with high-transmission jet sample and X-skimmer cones, resulting in a typical sensitivity of 3500–4000 V/ppm for Hf with a sample introduction rate of ~150 μL/min. Nine Faraday cups were set to monitor the isotopes ^{172}Yb, ^{174}Hf, ^{175}Lu, ^{176}Hf, ^{177}Hf, ^{178}Hf, ^{179}Hf, ^{180}Hf, and ^{182}W. Owing to the column chemistry, efficient separation of Hf was achieved, with interferences from Yb, Lu, and W found to be trivial. Data were acquired in the static mode over 60 cycles using an integration time of 8.4 s. Instrumental mass bias was corrected by normalizing the measured $^{179}Hf/^{177}Hf$ to 0.7325 using an exponential law. Mass bias corrected $^{176}Hf/^{177}Hf$ ratios were further normalized to the reference value of 0.282160 for the JMC-475 standard (Blichert-Toft et al., 1997). Analytical uncertainties in the Hf isotope ratios combined the internal precisions (2 SE) and the reproducibility (2 SD) of the JMC-Hf 475, added in quadrature (Table 3). The chondritic parameters reported by Iizuka et al. (2015) were used to calculate εHf values.

Table 1
LA-ICP-MS U—Pb isotopic analytical data for zircons from Taitao granitoids.

Sample No.	Analysis No.	Texture	$^{206}Pb/^{238}U$		2 SE	$^{207}Pb/^{235}U$ *1		2 SE	RHO *2	$^{206}Pb/^{238}U$Age (Ma)		2 SE	$^{207}Pb/^{235}U$Age (Ma)		2 SE	U (ppm)	Th (ppm)	Th/U	Analysis sequence
Cabo Raper Pluton																			
TPB56	2b	Inherited core	0.26496	±	0.00465	4.22640	±	0.23621	0.31	1515.2	±	23.7	1679.2	±	47.0	56	44	1.3	1
	3–2	Rim	0.00049	±	0.00006	b.d.l*	±			3.1	±	0.4		±		270	141	1.9	1
	4–2	Rim	0.00049	±	0.00008	b.d.l*	±			3.1	±	0.5		±		129	62	2.1	1
	6–2	Inherited core	0.00070	±	0.00007	b.d.l*	±			4.5	±	0.4		±		257	193	1.3	1
	7–2	Rim	0.00058	±	0.00005	0.00101	±	0.00083	0.11	3.7	±	0.3	1.0	±	0.8	339	204	1.7	1
	11a-2	Inherited core	0.00309	±	0.00013	0.02248	±	0.00414	0.22	19.9	±	0.8	22.6	±	4.1	349	227	1.5	1
	13–2	Rim	0.00059	±	0.00007	b.d.l*	±			3.8	±	0.4		±		218	79	2.7	1
	14–2	Inherited core	0.00054	±	0.00004	0.00361	±	0.00131	0.21	3.5	±	0.3	3.7	±	1.3	536	602	0.9	1
	16–2	Rim	0.00062	±	0.00006	0.00860	±	0.00269	0.29	4.0	±	0.4	8.7	±	2.7	304	200	1.5	1
	17–2	Rim	0.00061	±	0.00008	0.00979	±	0.00401	0.31	3.9	±	0.5	9.9	±	4.0	159	79	2.0	1
	18–2	Rim	0.00063	±	0.00011	0.00360	±	0.00315	0.20	4.1	±	0.7	3.7	±	3.2	83	29	2.9	1
	19a-2	Inherited core	0.00323	±	0.00026	0.01543	±	0.00684	0.18	20.8	±	1.7	15.5	±	6.9	81	37	2.2	1
	19b-2	Rim	0.00056	±	0.00009	0.00323	±	0.00275	0.20	3.6	±	0.6	3.3	±	2.8	106	27	3.9	1
	21–2	Rim	0.00057	±	0.00008	0.01466	±	0.00562	0.37	3.7	±	0.5	14.8	±	5.6	135	75	1.8	1
	22–2	Rim	0.00073	±	0.00007	b.d.l*	±			4.7	±	0.5		±		218	95	2.3	1
	23–2	Rim	0.00067	±	0.00007	0.00826	±	0.00310	0.28	4.3	±	0.4	8.3	±	3.1	215	78	2.8	1
	25–2	Magmatic core	0.00068	±	0.00006	0.00580	±	0.00226	0.24	4.4	±	0.4	5.9	±	2.3	269	156	1.7	1
	26–2	Magmatic core	0.00098	±	0.00007	0.00857	±	0.00260	0.24	6.3	±	0.5	8.7	±	2.6	305	289	1.1	1
	28–2	Magmatic core	0.00073	±	0.00006	0.00280	±	0.00137	0.16	4.7	±	0.4	2.8	±	1.4	332	353	0.9	1
	29b-2	Rim	0.00063	±	0.00007	0.00430	±	0.00215	0.21	4.0	±	0.4	4.4	±	2.2	216	59	3.6	1
	31	Rim	0.00053	±	0.00007	0.00733	±	0.00326	0.30	3.4	±	0.5	7.4	±	3.3	177	63	0.4	2
	33	Rim	0.00073	±	0.00009	0.00407	±	0.00239	0.20	4.7	±	0.6	4.1	±	2.4	164	72	0.4	2
	34	Rim	0.00057	±	0.00006	0.00440	±	0.00206	0.24	3.6	±	0.4	4.5	±	2.1	247	188	0.8	2
	35	Magmatic core	0.00075	±	0.00009	0.00936	±	0.00383	0.29	4.9	±	0.6	9.5	±	3.9	161	84	0.5	2
	36	Rim	0.00050	±	0.00006	0.00315	±	0.00162	0.22	3.2	±	0.4	3.2	±	1.6	279	267	1.0	2
	37	Magmatic core	0.00079	±	0.00008	0.00404	±	0.00206	0.20	5.1	±	0.5	4.1	±	2.1	218	83	0.4	2
	38	Magmatic core	0.00062	±	0.00008	0.00564	±	0.00295	0.25	4.0	±	0.5	5.7	±	3.0	156	106	0.7	2
	39	Rim	0.00072	±	0.00009	0.01140	±	0.00438	0.34	4.6	±	0.6	11.5	±	4.4	176	69	0.4	2
TPE88	1–2	Rim	0.00049	±	0.00465	0.01123	±	0.00391	0.35	3.2	±	0.4	11.3	±	3.9	239	135	1.8	1
	2–2	Rim	0.00050	±	0.00006	0.00535	±	0.00192	0.26	3.2	±	0.3	5.4	±	1.9	412	290	1.4	1
	3–2	Magmatic core	0.00059	±	0.00008	0.00230	±	0.00116	0.16	3.8	±	0.3	2.3	±	1.2	436	399	1.1	1
	4–2	Rim	0.00085	±	0.00007	b.d.l*	±			5.5	±	0.9		±		81	30	2.7	1
	5a-2	Rim	0.00068	±	0.00005	0.00017	±	0.00041	0.04	4.4	±	0.5	0.2	±	0.4	241	131	1.8	1
	7–2	Magmatic core	0.00052	±	0.00013	0.00603	±	0.00288	0.27	3.4	±	0.4	6.1	±	2.9	206	137	1.5	1
	8–2	Inherited core	0.00050	±	0.00007	0.00729	±	0.00302	0.30	3.2	±	0.4	7.4	±	3.0	237	106	2.2	1
	10–2	Rim	0.00073	±	0.00004	0.00122	±	0.00115	0.11	4.7	±	0.5	1.2	±	1.2	230	134	1.7	1
	11–2	Magmatic core	0.00052	±	0.00006	0.00180	±	0.00134	0.16	3.3	±	0.4	1.8	±	1.4	236	146	1.6	1
	12–2	Rim	0.00072	±	0.00008	0.00028	±	0.00070	0.05	4.7	±	0.6	0.3	±	0.7	141	54	2.6	1
	15a-2	Magmatic core	0.00052	±	0.00011	0.00433	±	0.00162	0.23	3.3	±	0.3	4.4	±	1.6	454	155	2.9	1
	16–2	Rim	0.00063	±	0.00026	0.00476	±	0.00146	0.23	4.0	±	0.3	4.8	±	1.5	556	629	0.9	1
	18–2	Inherited core	0.00270	±	0.00009	0.02416	±	0.00362	0.25	17.4	±	0.6	24.2	±	3.6	486	284	1.7	1
	19–2	Magmatic core	0.00054	±	0.00008	0.00626	±	0.00279	0.27	3.4	±	0.4	6.3	±	2.8	209	110	1.9	1
	21	Inherited core	0.01132	±	0.00007	0.07988	±	0.01228	0.22	72.6	±	2.5	78.0	±	11.6	136	78	1.7	1
	22	Rim	0.00064	±	0.00007	0.00172	±	0.00127	0.14	4.1	±	0.4	1.7	±	1.3	248	209	1.2	1
	23	Rim	0.00069	±	0.00006	0.00889	±	0.00399	0.28	4.5	±	0.6	9.0	±	4.0	148	64	2.3	1
	24	Rim	0.00061	±	0.00007	0.00219	±	0.00162	0.16	3.9	±	0.5	2.2	±	1.6	195	122	1.6	1
	25	Inherited core	0.00309	±	0.00006	0.03760	±	0.00972	0.28	19.9	±	1.4	37.5	±	9.6	106	99	1.1	1
	26	Rim	0.00072	±	0.00007	0.00145	±	0.00106	0.12	4.6	±	0.4	1.5	±	1.1	293	154	1.9	1
	27	Magmatic core	0.00079	±	0.00007	0.00412	±	0.00251	0.19	5.1	±	0.6	4.2	±	2.5	181	70	2.6	1
	28	Magmatic core	0.00066	±	0.00009	0.00355	±	0.00216	0.19	4.3	±	0.5	3.6	±	2.2	211	165	1.3	1
	29	Rim	0.00076	±	0.00006	0.00352	±	0.00214	0.18	4.9	±	0.5	3.6	±	2.2	212	160	1.3	1
	30	Rim	0.00057	±	0.00009	0.00959	±	0.00281	0.32	3.7	±	0.3	9.7	±	2.8	398	238	1.7	1

(continued on next page)

Table 1 (*continued*)

Sample No.	Analysis No.	Texture	$^{206}Pb/^{238}U$		2 SE	$^{207}Pb/^{235}U$ *1		2 SE	RHO *2	$^{206}Pb/^{238}U$Age (Ma)		2 SE	$^{207}Pb/^{235}U$Age (Ma)		2 SE	U (ppm)	Th (ppm)	Th/U	Analysis sequence
	31	Magmatic core	0.00068	±	0.00006	0.00269	±	0.00099	0.17	4.4	±	0.3	2.7	±	1.0	753	933	0.8	1
	32	Magmatic core	0.00070	±	0.00008	0.00207	±	0.00153	0.15	4.5	±	0.5	2.1	±	1.6	237	107	2.2	1
	33	Magmatic core	0.00056	±	0.00008	0.00179	±	0.00133	0.15	3.6	±	0.4	1.8	±	1.3	274	171	1.6	1
	34	Rim	0.00066	±	0.00009	0.00160	±	0.00118	0.13	4.3	±	0.4	1.6	±	1.2	306	141	2.2	1
	35	Magmatic core	0.00062	±	0.00465	0.00129	±	0.00077	0.13	4.0	±	0.3	1.3	±	0.8	578	562	1.0	1
	36	Rim	0.00070	±	0.00006	0.00370	±	0.00195	0.19	4.5	±	0.5	3.8	±	2.0	271	118	2.3	1
	37	Magmatic core	0.00066	±	0.00008	0.00806	±	0.00234	0.28	4.2	±	0.3	8.2	±	2.4	377	365	1.0	2
	38	Rim	0.00065	±	0.00007	0.00688	±	0.00295	0.26	4.2	±	0.5	7.0	±	3.0	195	97	0.5	2
	39	Rim	0.00060	±	0.00005	0.00630	±	0.00165	0.26	3.9	±	0.3	6.4	±	1.7	583	661	1.1	2
	40	magmatic core	0.00060	±	0.00013	0.00396	±	0.00166	0.21	3.9	±	0.3	4.0	±	1.7	339	254	0.7	2
	41	magmatic core	0.00055	±	0.00007	0.00366	±	0.00211	0.21	3.5	±	0.4	3.7	±	2.1	193	102	0.5	2
	42	Magmatic core	0.00074	±	0.00004	0.00723	±	0.00287	0.25	4.7	±	0.5	7.3	±	2.9	215	152	0.7	2
	43	Rim	0.00065	±	0.00006	0.00284	±	0.00161	0.18	4.2	±	0.4	2.9	±	1.6	249	102	0.4	2
	44	Rim	0.00066	±	0.00008	0.00422	±	0.00164	0.21	4.2	±	0.3	4.3	±	1.7	368	106	0.3	2
TPE90	4a-2	Magmatic core	0.00064	±	0.00011	0.00352	±	0.00249	0.19	4.1	±	0.6	3.6	±	2.5	154	91	1.7	1
	7–2	Rim	0.00060	±	0.00026	0.00797	±	0.00351	0.28	3.9	±	0.5	8.1	±	3.5	193	97	2.0	1
	8–2	Rim	0.00056	±	0.00009	0.00029	±	0.00071	0.06	3.6	±	0.5	0.3	±	0.7	144	75	1.9	1
	10b	Rim	0.00052	±	0.00008	b.d.l*	±			3.3	±	0.5		±		169	87	1.9	1
	11c	Rim	0.00061	±	0.00007	b.d.l*	±			4.0	±	0.5		±		202	91	2.2	1
	13–2	Rim	0.00046	±	0.00007	0.00143	±	0.00135	0.15	3.0	±	0.4	1.4	±	1.4	204	88	2.3	1
	15–2	Rim	0.00057	±	0.00006	0.00361	±	0.00256	0.21	3.7	±	0.5	3.7	±	2.6	150	113	1.3	1
	16c-2	Rim	0.00053	±	0.00007	0.00958	±	0.00340	0.32	3.4	±	0.4	9.7	±	3.4	265	207	1.3	1
	20a-2	Inherited core	0.00066	±	0.00006	0.00508	±	0.00225	0.23	4.2	±	0.4	5.1	±	2.3	296	144	2.1	1
	20c	Rim	0.00072	±	0.00007	0.01180	±	0.00493	0.31	4.6	±	0.6	11.9	±	5.0	152	102	1.5	1
	22b-2	Rim	0.00063	±	0.00007	0.00656	±	0.00364	0.26	4.1	±	0.6	6.6	±	3.7	150	67	2.2	1
	26–2	Rim	0.00069	±	0.00009	0.00702	±	0.00256	0.26	4.4	±	0.4	7.1	±	2.6	326	353	0.9	1
	28–2	Rim	0.00062	±	0.00006	0.01247	±	0.00401	0.34	4.0	±	0.4	12.6	±	4.0	268	143	1.9	1
	30–2	Rim	0.00070	±	0.00009	0.01044	±	0.00530	0.30	4.5	±	0.7	10.5	±	5.3	119	45	2.6	1
	31a-2	Magmatic core	0.00073	±	0.00006	0.00315	±	0.00245	0.17	4.7	±	0.6	3.2	±	2.5	146	87	1.7	1
	31b-2	Rim	0.00065	±	0.00008	0.00668	±	0.00371	0.26	4.2	±	0.6	6.8	±	3.7	147	69	2.1	1
	33–2	Rim	0.00058	±	0.00008	0.00545	±	0.00267	0.25	3.7	±	0.5	5.5	±	2.7	228	157	1.5	1
	34–2	Rim	0.00062	±	0.00009	0.01582	±	0.00630	0.37	4.0	±	0.6	15.9	±	6.3	145	62	2.3	1
	36b-2	Inherited core	0.00053	±	0.00465	0.00373	±	0.00296	0.22	3.4	±	0.6	3.8	±	3.0	123	35	3.5	1
	41	Magmatic core	0.00065	±	0.00006	0.00357	±	0.00118	0.20	4.2	±	0.3	3.6	±	1.2	570	552	1.0	1
	42	Rim	0.00072	±	0.00008	0.00443	±	0.00190	0.21	4.7	±	0.4	4.5	±	1.9	276	124	2.2	1
	43	Rim	0.00060	±	0.00007	0.00190	±	0.00137	0.15	3.9	±	0.4	1.9	±	1.4	215	87	2.5	1
	44	Rim	0.00057	±	0.00005	b.d.l*	±			3.6	±	0.4		±		198	103	1.9	1
	45	Magmatic core	0.00056	±	0.00013	0.00262	±	0.00191	0.18	3.6	±	0.5	2.7	±	1.9	156	117	1.3	1
	46	Core	0.00055	±	0.00007	0.01275	±	0.00525	0.36	3.5	±	0.5	12.9	±	5.3	128	66	1.9	1
	47	Rim	0.00054	±	0.00004	0.01249	±	0.00460	0.36	3.5	±	0.5	12.6	±	4.6	163	75	2.2	1
	48	Rim	0.00071	±	0.00006	0.01387	±	0.00365	0.34	4.6	±	0.4	14.0	±	3.7	279	130	2.1	1
	49	Rim	0.00052	±	0.00008	0.00722	±	0.00214	0.30	3.3	±	0.3	7.3	±	2.2	395	143	2.8	1
	50	Rim	0.00087	±	0.00011	0.02569	±	0.00934	0.39	5.6	±	0.8	25.8	±	9.3	87	36	2.4	1
	51	Rim	0.00067	±	0.00026	0.00747	±	0.00279	0.28	4.3	±	0.5	7.6	±	2.8	240	159	0.7	2
	54	Magmatic core	0.00063	±	0.00009	0.00313	±	0.00172	0.20	4.1	±	0.4	3.2	±	1.7	239	174	0.7	2
	57	Magmatic core	0.00067	±	0.00008	0.00529	±	0.00115	0.29	4.3	±	0.3	5.4	±	1.2	1010	1606	1.6	2
	59	Rim	0.00062	±	0.00007	0.00931	±	0.00405	0.31	4.0	±	0.5	9.4	±	4.1	148	105	0.7	2
	60	Rim	0.00072	±	0.00007	0.00974	±	0.00295	0.31	4.7	±	0.4	9.8	±	3.0	291	150	0.5	2
	63	Rim	0.00063	±	0.00006	0.00213	±	0.00148	0.24	4.0	±	0.7	2.2	±	1.5	235	68	0.3	2
	64	Rim	0.00057	±	0.00007	0.00606	±	0.00272	0.37	3.7	±	0.6	6.1	±	2.7	229	106	0.5	2
Cabo Raper Pluton					Average for magmatic core and rim					4.1	±	1.2							
Estero Cono Pluton																			
TPE135	4–2	Magmatic core	0.00078	±	0.00006	0.00212	±	0.00118	0.14	5.0	±	0.4	2.1	±	1.2	485	251	1.9	1
	5a-2	Magmatic core	0.00082	±	0.00009	0.01517	±	0.00509	0.33	5.3	±	0.6	15.3	±	5.1	230	132	1.7	1
	5b-2	rim	0.00088	±	0.00008	0.00545	±	0.00247	0.21	5.6	±	0.5	5.5	±	2.5	301	148	2.0	1

	7–2	Rim	0.00081	±	0.00009	0.01226	±	0.00445	0.30	5.2	±	0.6	12.4	±	4.5	235	76	3.1	1
	8–2	Rim	0.00081	±	0.00005	0.00388	±	0.00140	0.18	5.2	±	0.3	3.9	±	1.4	661	431	1.5	1
	9–2	Rim	0.00076	±	0.00006	0.00547	±	0.00189	0.22	4.9	±	0.4	5.5	±	1.9	526	273	1.9	1
	10–2	Rim	0.00086	±	0.00006	0.00787	±	0.00240	0.25	5.5	±	0.4	8.0	±	2.4	483	234	2.1	1
	11–2	Rim	0.00074	±	0.00007	0.00234	±	0.00157	0.15	4.7	±	0.5	2.4	±	1.6	307	154	2.0	1
	12a-2	magmatic core	0.00083	±	0.00006	0.00733	±	0.00230	0.24	5.3	±	0.4	7.4	±	2.3	453	260	1.7	1
	14b	Magmatic core	0.00084	±	0.00007	0.00792	±	0.00275	0.25	5.4	±	0.5	8.0	±	2.8	346	266	1.3	1
	17–2	Rim	0.00078	±	0.00005	0.00581	±	0.00156	0.22	5.0	±	0.3	5.9	±	1.6	771	799	1.0	1
	18–2	Rim	0.00086	±	0.00005	0.00971	±	0.00213	0.27	5.5	±	0.3	9.8	±	2.1	729	434	1.7	1
	19–2	Rim	0.00073	±	0.00004	0.00559	±	0.00131	0.23	4.7	±	0.2	5.7	±	1.3	1060	1030	1.0	1
	20–2	Magmatic core	0.00080	±	0.00006	0.00965	±	0.00267	0.27	5.2	±	0.4	9.7	±	2.7	464	153	3.0	1
	21–2	Rim	0.00072	±	0.00006	0.00031	±	0.00044	0.06	4.7	±	0.4	0.3	±	0.5	461	250	1.8	1
	23a-2	Magmatic core	0.00066	±	0.00005	0.00326	±	0.00144	0.18	4.3	±	0.3	3.3	±	1.5	487	244	2.0	1
	27b-2	Inherited core	0.00068	±	0.00011	0.01466	±	0.00669	0.35	4.4	±	0.7	14.8	±	6.7	133	58	2.3	1
	30–2	Magmatic core	0.00090	±	0.00007	0.00530	±	0.00217	0.20	5.8	±	0.5	5.4	±	2.2	354	242	1.5	1
	35b	Magmatic core	0.00075	±	0.00008	0.00164	±	0.00136	0.12	4.8	±	0.5	1.7	±	1.4	265	183	1.4	1
	38–2	Inherited core	0.00074	±	0.00006	0.00897	±	0.00258	0.28	4.8	±	0.4	9.1	±	2.6	493	244	2.0	1
	41	Magmatic core	0.00084	±	0.00006	0.00396	±	0.00164	0.18	5.4	±	0.4	4.0	±	1.7	433	289	1.5	1
	42	Rim	0.00078	±	0.00006	0.00507	±	0.00197	0.21	5.0	±	0.4	5.1	±	2.0	393	164	2.4	1
	43	Inherited core	0.00087	±	0.00008	0.01392	±	0.00385	0.31	5.6	±	0.5	14.0	±	3.9	321	201	1.6	1
	44	Magmatic core	0.00083	±	0.00009	0.00165	±	0.00149	0.12	5.4	±	0.6	1.7	±	1.5	209	88	2.4	1
	46	Magmatic core	0.00075	±	0.00009	0.00350	±	0.00241	0.18	4.8	±	0.6	3.5	±	2.4	177	87	2.0	1
	47	Magmatic core	0.00081	±	0.00008	0.00498	±	0.00252	0.21	5.2	±	0.5	5.0	±	2.6	234	153	1.5	1
	48	Magmatic core	0.00077	±	0.00007	0.00606	±	0.00256	0.23	4.9	±	0.5	6.1	±	2.6	283	109	2.6	1
	49	Rim	0.00074	±	0.00007	0.00685	±	0.00254	0.25	4.8	±	0.4	6.9	±	2.6	331	109	3.0	1
	50	Magmatic core	0.00073	±	0.00007	0.00329	±	0.00165	0.18	4.7	±	0.4	3.3	±	1.7	355	181	2.0	1
	51	Magmatic core	0.00071	±	0.00006	0.00623	±	0.00224	0.24	4.5	±	0.4	6.3	±	2.3	410	141	2.9	1
	52	Rim	0.00069	±	0.00007	0.00889	±	0.00311	0.28	4.5	±	0.4	9.0	±	3.1	320	99	3.2	1
	53	Magmatic core	0.00074	±	0.00007	0.01208	±	0.00352	0.31	4.8	±	0.4	12.2	±	3.5	355	234	1.5	1
	54	Magmatic core	0.00073	±	0.00003	0.00607	±	0.00113	0.25	4.7	±	0.2	6.1	±	1.1	1610	1945	0.8	1
	56	Rim	0.00089	±	0.00008	0.00326	±	0.00170	0.17	5.7	±	0.5	3.3	±	1.7	245	125	0.5	2
	60	Rim	0.00087	±	0.00007	0.00521	±	0.00195	0.22	5.6	±	0.5	5.3	±	2.0	310	160	0.5	2
	61	Rim	0.00079	±	0.00005	0.00443	±	0.00101	0.26	5.1	±	0.3	4.5	±	1.0	1007	873	0.9	2
	62	Rim	0.00079	±	0.00006	0.00709	±	0.00187	0.28	5.1	±	0.4	7.2	±	1.9	486	295	0.6	2
	64	Magmatic core	0.00082	±	0.00010	0.00856	±	0.00351	0.30	5.3	±	0.7	8.7	±	3.5	179	91	0.5	2
	65	Magmatic core	0.00079	±	0.00009	0.00460	±	0.00222	0.24	5.1	±	0.6	4.7	±	2.2	232	83	0.4	2
Estero Cono Pluton					Average for magmatic core and rim					5.1	±	0.7							
Bahia Barrientos Intrusion																			
TPB243	1a-2	Rim	0.00078	±	0.00005	0.00105	±	0.00070	0.10	5.1	±	0.3	1.1	±	0.7	597	182	3.3	1
	1b-2	Rim	0.00081	±	0.00007	0.00566	±	0.00232	0.22	5.2	±	0.5	5.7	±	2.3	435	135	3.2	1
	6a-2	Rim	0.00070	±	0.00005	0.00654	±	0.00170	0.25	4.5	±	0.3	6.6	±	1.7	711	176	4.0	1
	6b-2	Rim	0.00073	±	0.00003	0.00462	±	0.00090	0.22	4.7	±	0.2	4.7	±	0.9	1761	610	2.9	1
	9–2	Rim	0.00077	±	0.00004	0.00226	±	0.00081	0.15	5.0	±	0.3	2.3	±	0.8	989	315	3.1	1
	10b-1	Rim	0.00077	±	0.00005	0.00225	±	0.00100	0.15	5.0	±	0.3	2.3	±	1.0	636	231	2.8	1
	10c	Rim	0.00074	±	0.00004	0.00436	±	0.00125	0.21	4.8	±	0.3	4.4	±	1.3	1160	514	2.3	1
	11–2	Rim	0.00077	±	0.00005	0.00584	±	0.00165	0.23	4.9	±	0.3	5.9	±	1.7	659	301	2.2	1
	12–2	Rim	0.00085	±	0.00006	0.00342	±	0.00141	0.17	5.5	±	0.4	3.5	±	1.4	497	174	2.9	1
	17–2	Magmatic core	0.00067	±	0.00005	0.00595	±	0.00168	0.25	4.3	±	0.3	6.0	±	1.7	912	248	3.7	1
	22	Rim	0.00077	±	0.00005	0.00662	±	0.00170	0.25	5.0	±	0.3	6.7	±	1.7	986	435	2.3	1
	23	Magmatic core	0.00079	±	0.00005	0.00265	±	0.00106	0.16	5.1	±	0.3	2.7	±	1.1	931	423	2.2	1
	25	Rim	0.00072	±	0.00003	0.00443	±	0.00091	0.22	4.6	±	0.2	4.5	±	0.9	2311	990	2.3	1
	26	Magmatic core	0.00081	±	0.00007	0.00286	±	0.00154	0.16	5.2	±	0.5	2.9	±	1.6	473	180	2.6	1
	27	Magmatic core	0.00073	±	0.00005	0.00391	±	0.00126	0.20	4.7	±	0.3	4.0	±	1.3	1008	397	2.5	1
	28	Rim	0.00067	±	0.00004	0.00486	±	0.00124	0.23	4.3	±	0.3	4.9	±	1.3	1343	802	1.7	1
Bahia Barrientos Intrusion					Average for magmatic core and rim					4.9	±	0.7							
Tres Montes Pluton																			

(continued on next page)

Table 1 (*continued*)

Sample No.	Analysis No.	Texture	$^{206}Pb/^{238}U$		2 SE	$^{207}Pb/^{235}U$ *1		2 SE	RHO *2	$^{206}Pb/^{238}U$Age (Ma)		2 SE	$^{207}Pb/^{235}U$Age (Ma)		2 SE	U (ppm)	Th (ppm)	Th/U	Analysis sequence
TPH75	1–2	Magmatic core	0.00089	±	0.00008	0.00307	±	0.00165	0.16	5.7	±	0.5	3.1	±	1.7	404	161	2.5	1
	2b	Magmatic core	0.00081	±	0.00013	0.00970	±	0.00552	0.28	5.2	±	0.8	9.8	±	5.6	105	69	1.5	1
	3c	Rim	0.00086	±	0.00006	0.00476	±	0.00180	0.20	5.6	±	0.4	4.8	±	1.8	448	501	0.9	1
	3d	Magmatic core	0.00085	±	0.00005	0.00488	±	0.00145	0.20	5.5	±	0.3	4.9	±	1.5	877	875	1.0	1
	5–2	Rim	0.00100	±	0.00010	0.00939	±	0.00390	0.25	6.4	±	0.7	9.5	±	3.9	197	136	1.5	1
	7–2	Inherited core	0.00089	±	0.00004	0.00785	±	0.00119	0.26	5.7	±	0.2	7.9	±	1.2	1865	1888	1.0	1
	11b	Magmatic core	0.00105	±	0.00012	0.00941	±	0.00423	0.24	6.8	±	0.7	9.5	±	4.3	167	137	1.2	1
	13b	Magmatic core	0.00076	±	0.00007	0.01160	±	0.00351	0.31	4.9	±	0.5	11.7	±	3.5	328	364	0.9	1
	15–2	Magmatic core	0.00084	±	0.00010	0.01676	±	0.00618	0.34	5.4	±	0.7	16.9	±	6.2	160	137	1.2	1
	16–2	Inherited core	0.00091	±	0.00003	0.00524	±	0.00090	0.22	5.9	±	0.2	5.3	±	0.9	2050	1232	1.7	1
	18–2	Rim	0.00088	±	0.00006	0.00821	±	0.00205	0.25	5.7	±	0.4	8.3	±	2.1	633	442	1.4	1
	19b	Inherited core	0.00085	±	0.00003	0.00327	±	0.00074	0.18	5.5	±	0.2	3.3	±	0.8	2239	1840	1.2	1
	21	Magmatic core	0.00097	±	0.00006	0.00345	±	0.00122	0.16	6.2	±	0.4	3.5	±	1.2	847	974	0.9	1
	22	Magmatic core	0.00085	±	0.00009	0.01319	±	0.00452	0.31	5.5	±	0.6	13.3	±	4.5	273	190	1.4	1
	23	Magmatic core	0.00087	±	0.00004	0.00425	±	0.00107	0.19	5.6	±	0.3	4.3	±	1.1	1403	945	1.5	1
	24	Rim	0.00079	±	0.00009	0.00734	±	0.00331	0.25	5.1	±	0.6	7.4	±	3.3	261	166	1.6	1
	25	Rim	0.00065	±	0.00010	0.00511	±	0.00332	0.23	4.2	±	0.6	5.2	±	3.4	176	109	1.6	1
	26	Inherited core	0.01577	±	0.00039	0.09905	±	0.00957	0.26	100.9	±	2.5	95.9	±	8.9	561	385	1.5	1
	27	Inherited core	0.09295	±	0.00173	0.77240	±	0.04220	0.34	573.0	±	10.2	581.1	±	24.5	1657	715	2.3	1
	28	Magmatic core	0.00086	±	0.00006	0.00619	±	0.00183	0.23	5.5	±	0.4	6.3	±	1.8	599	542	1.1	1
	29	Rim	0.00090	±	0.00008	0.00266	±	0.00162	0.15	5.8	±	0.5	2.7	±	1.6	308	200	1.5	1
	30	Magmatic core	0.00105	±	0.00012	0.01911	±	0.00689	0.33	6.8	±	0.8	19.2	±	6.9	149	117	1.3	1
	31	Rim	0.00072	±	0.00009	0.01019	±	0.00430	0.29	4.6	±	0.6	10.3	±	4.3	194	112	1.7	1
	32	Magmatic core	0.00085	±	0.00007	0.00862	±	0.00260	0.26	5.5	±	0.4	8.7	±	2.6	430	297	1.4	1
	33	Rim	0.00075	±	0.00007	0.00657	±	0.00250	0.24	4.9	±	0.4	6.7	±	2.5	344	356	1.0	1
Tres Montes Pluton					Average for magmatic core and rim					5.5	±	1.3							
Seno Hoppner Pluton																			
TPG171	1b-2	Magmatic core	0.00088	±	0.00004	0.00639	±	0.00126	0.23	5.7	±	0.3	6.5	±	1.3	1221	1615	0.8	1
	3–2	Magmatic core	0.00074	±	0.00004	0.00432	±	0.00129	0.20	4.8	±	0.3	4.4	±	1.3	737	815	0.9	1
	4–2	Magmatic core	0.00089	±	0.00004	0.00411	±	0.00097	0.19	5.7	±	0.3	4.2	±	1.0	1043	1394	0.7	1
	8–2	Magmatic core	0.00089	±	0.00005	0.00662	±	0.00169	0.23	5.7	±	0.3	6.7	±	1.7	580	567	1.0	1
	9–2	Magmatic core	0.00077	±	0.00005	0.00953	±	0.00200	0.29	5.0	±	0.3	9.6	±	2.0	637	603	1.1	1
	11–2	Rim	0.00085	±	0.00008	0.00853	±	0.00303	0.26	5.5	±	0.5	8.6	±	3.1	240	171	1.4	1
	12–2	Magmatic core	0.00085	±	0.00006	0.00382	±	0.00138	0.18	5.5	±	0.4	3.9	±	1.4	479	462	1.0	1
	13–2	Magmatic core	0.00087	±	0.00004	0.00338	±	0.00100	0.17	5.6	±	0.3	3.4	±	1.0	804	1122	0.7	1
	14–2	Magmatic core	0.00078	±	0.00005	0.00236	±	0.00090	0.15	5.0	±	0.3	2.4	±	0.9	680	826	0.8	1
	15b	Magmatic core	0.00089	±	0.00004	0.00491	±	0.00100	0.21	5.7	±	0.2	5.0	±	1.0	1192	1556	0.8	1
	16b	Rim	0.00086	±	0.00005	0.00585	±	0.00153	0.22	5.5	±	0.3	5.9	±	1.5	618	631	1.0	1
	19b	Magmatic core	0.00078	±	0.00004	0.00316	±	0.00090	0.17	5.0	±	0.2	3.2	±	0.9	1089	1354	0.8	1
	20–2	Magmatic core	0.00082	±	0.00004	0.00455	±	0.00110	0.20	5.3	±	0.3	4.6	±	1.1	1095	1303	0.8	1
	21a-2	Magmatic core	0.00082	±	0.00004	0.00733	±	0.00162	0.24	5.3	±	0.3	7.4	±	1.6	855	898	1.0	1
	22–2	Magmatic core	0.00090	±	0.00005	0.00646	±	0.00150	0.22	5.8	±	0.3	6.5	±	1.5	851	870	1.0	1
	23a-2	Magmatic core	0.00086	±	0.00004	0.00762	±	0.00130	0.26	5.6	±	0.2	7.7	±	1.3	1149	1686	0.7	1
	24–2	Magmatic core	0.00080	±	0.00003	0.00576	±	0.00103	0.23	5.2	±	0.2	5.8	±	1.0	1669	2658	0.6	1
	25–2	Rim	0.00091	±	0.00005	0.00783	±	0.00192	0.24	5.9	±	0.3	7.9	±	1.9	637	511	1.2	1
	26–2	Rim	0.00085	±	0.00004	0.00697	±	0.00136	0.24	5.5	±	0.3	7.1	±	1.4	1157	1644	0.7	1
	27–2	Magmatic core	0.00087	±	0.00005	0.00723	±	0.00159	0.24	5.6	±	0.3	7.3	±	1.6	867	885	1.0	1
	31	Magmatic core	0.00088	±	0.00004	0.00634	±	0.00103	0.26	5.6	±	0.2	6.4	±	1.0	2326	2687	0.9	1
	32	Magmatic core	0.00085	±	0.00004	0.00477	±	0.00108	0.22	5.5	±	0.3	4.8	±	1.1	1513	1953	0.8	1
	33	Rim	0.00093	±	0.00005	0.00591	±	0.00147	0.23	6.0	±	0.3	6.0	±	1.5	1001	972	1.0	1
	34	Magmatic core	0.00081	±	0.00004	0.00706	±	0.00138	0.26	5.3	±	0.3	7.1	±	1.4	1439	1656	0.9	1
	35	Rim	0.00086	±	0.00005	0.00535	±	0.00130	0.23	5.5	±	0.3	5.4	±	1.3	1166	974	1.2	1
	36	Magmatic core	0.00090	±	0.00005	0.00725	±	0.00174	0.25	5.8	±	0.3	7.3	±	1.8	906	781	1.2	1
	37	Magmatic core	0.00084	±	0.00004	0.00541	±	0.00123	0.23	5.4	±	0.3	5.5	±	1.2	1334	1515	0.9	1
	38	Rim	0.00081	±	0.00006	0.00623	±	0.00184	0.24	5.2	±	0.4	6.3	±	1.9	687	461	1.5	1

	39	Magmatic core	0.00076	±	0.00006	0.00501	±	0.00167	0.22	4.9	±	0.4	5.1	±	1.7	658	521	1.3	1
	40	Magmatic core	0.00087	±	0.00005	0.00629	±	0.00150	0.24	5.6	±	0.3	6.4	±	1.5	1044	983	1.1	1
	41	Magmatic core	0.00085	±	0.00005	0.00939	±	0.00158	0.33	5.5	±	0.3	9.5	±	1.6	1049	1326	1.3	2
	42	Magmatic core	0.00074	±	0.00006	0.00870	±	0.00236	0.29	4.8	±	0.4	8.8	±	2.4	418	282	0.7	2
	43	Rim	0.00070	±	0.00005	0.00699	±	0.00193	0.28	4.5	±	0.3	7.1	±	2.0	488	456	0.9	2
	44	Magmatic core	0.00083	±	0.00006	0.00493	±	0.00154	0.23	5.4	±	0.4	5.0	±	1.6	511	454	0.9	2
	45	Magmatic core	0.00074	±	0.00005	0.00404	±	0.00116	0.22	4.8	±	0.3	4.1	±	1.2	733	843	1.1	2
	46	Magmatic core	0.00083	±	0.00005	0.00897	±	0.00163	0.32	5.4	±	0.3	9.1	±	1.6	926	1191	1.3	2
	47	Rim	0.00076	±	0.00005	0.00593	±	0.00148	0.26	4.9	±	0.3	6.0	±	1.5	688	752	1.1	2
	48	Magmatic core	0.00076	±	0.00005	0.00429	±	0.00140	0.22	4.9	±	0.4	4.3	±	1.4	536	472	0.9	2
	49	Magmatic core	0.00087	±	0.00008	0.00306	±	0.00173	0.17	5.6	±	0.5	3.1	±	1.7	242	191	0.8	2
TPD116	4–2	Rim	0.00086	±	0.00005	0.00693	±	0.00160	0.24	5.6	±	0.3	7.0	±	1.6			1.6	1
	6–2	Rim	0.00094	±	0.00007	0.00089	±	0.00080	0.08	6.1	±	0.5	0.9	±	0.8	777	494	1.6	1
	8–2	magmatic core	0.00086	±	0.00009	0.00252	±	0.00172	0.15	5.5	±	0.5	2.6	±	1.7	358	224	1.7	1
	9–2	Rim	0.00078	±	0.00005	0.01080	±	0.00234	0.30	5.0	±	0.3	10.9	±	2.4	226	130	1.8	1
	10–2	Rim	0.00078	±	0.00004	0.00148	±	0.00065	0.12	5.0	±	0.3	1.5	±	0.7	616	348	1.5	1
	12–2	Rim	0.00081	±	0.00005	0.00431	±	0.00128	0.20	5.2	±	0.3	4.4	±	1.3	902	602	1.7	1
	13–2	Rim	0.00077	±	0.00007	0.00861	±	0.00307	0.27	5.0	±	0.5	8.7	±	3.1	721	423	2.2	1
	15–2	Rim	0.00088	±	0.00006	0.00452	±	0.00144	0.20	5.7	±	0.4	4.6	±	1.5	272	123	1.3	1
	17–2	Rim	0.00083	±	0.00004	0.00607	±	0.00119	0.25	5.3	±	0.3	6.1	±	1.2	820	613	0.9	1
	18–2	Magmatic core	0.00077	±	0.00005	0.00406	±	0.00139	0.20	5.0	±	0.3	4.1	±	1.4	1730	2034	1.4	1
	19–2	Rim	0.00083	±	0.00006	0.01193	±	0.00302	0.30	5.3	±	0.4	12.0	±	3.0	577	400	1.9	1
	21	Magmatic core	0.00078	±	0.00007	0.00671	±	0.00255	0.24	5.0	±	0.5	6.8	±	2.6	409	215	1.7	1
	22	Rim	0.00076	±	0.00006	0.00460	±	0.00162	0.21	4.9	±	0.4	4.7	±	1.6	400	237	1.9	1
	23	Rim	0.00078	±	0.00007	0.00627	±	0.00254	0.24	5.0	±	0.5	6.4	±	2.6	658	352	1.9	1
	24	Magmatic core	0.00113	±	0.00008	0.03783	±	0.00619	0.42	7.3	±	0.5	37.7	±	6.1	374	199	2.1	1
	25	Magmatic core	0.00087	±	0.00005	0.00708	±	0.00152	0.26	5.6	±	0.3	7.2	±	1.5	555	262	1.3	1
	26	Rim	0.00074	±	0.00007	0.00155	±	0.00114	0.13	4.8	±	0.4	1.6	±	1.2	1243	972	2.1	1
	27	Rim	0.00082	±	0.00005	0.00464	±	0.00132	0.22	5.3	±	0.3	4.7	±	1.3	421	204	2.3	1
	28	Rim	0.00070	±	0.00009	0.00466	±	0.00126	0.50	4.5	±	0.6	4.7	±	1.3	1018	437	1.1	2
	29	Rim	0.00071	±	0.00011	0.00731	±	0.00274	0.41	4.6	±	0.7	7.4	±	2.8	917	996	0.4	2
	30	Magmatic core	0.00074	±	0.00010	0.00664	±	0.00200	0.47	4.8	±	0.7	6.7	±	2.0	281	108	0.9	2
	31	Rim	0.00074	±	0.00012	0.01047	±	0.00383	0.44	4.8	±	0.8	10.6	±	3.9	510	435	0.5	2
Seno Hoppner Pluton					Average for magmatic core and rim					5.3	±	0.9							

*1 b.d.l. means below detection limit.
*2 RHO is coefficient of radiogenic 207Pb/235 U vs. 206Pb/238 U ratios.

Table 2
Oxygen isotope ratios of zircons in the Taitao granitoids measured with SIMS.

Analysis number	$\delta^{18}O$ (Zrc)	2 SD	Texture[a]	Analysis number	$\delta^{18}O$ (Zrc)	2 SD	Texture[a]	Analysis number	$\delta^{18}O$ (Zrc)	2 SD	Texture[a]	Analysis number	$\delta^{18}O$ (Zrc)	2 SD	Texture[a]	Analysis number	$\delta^{18}O$ (Zrc)	2 SD	Texture[a]	Analysis Number	$\delta^{18}O$ (Zrc)	2 SD	Texture[a]	Analysis Number	$\delta^{18}O$ (Zrc)	2 SD	Texture[a]	Analysis Number	$\delta^{18}O$ (Zrc)	2 SD	Texture[a]
Cabo Raper Pluton												Estero Cono Pluton				Bahia Barrientos Intrusion				Tres Montes Pluton				Seno Hoppner Pluton							
TPB56				*TPE88*				*TPE90*				*TPE135*				*TPB243*				*TPH75*				*TPG171*				*TPD116*			
1.0	6.0	0.1	Rim	1–1	6.3	0.1	Rim	1	6.2	0.3	Core	1–1	6.3	0.1	Core	1a-1	6.5	0.2	Rim	1–1	6.6	0.2	Rim	1a-1	5.4	0.2	Core	1	5.4	0.2	Rim
2a	6.0	0.1	Inherited	2–1	6.3	0.1	Rim	2	6.3	0.3	Rim	2	6.1	0.1	Rim	1b-1	6.6	0.2	Rim	2–1	6.4	0.2	Rim	1b-1	5.5	0.2	Core	2	5.5	0.2	Rim
3–1	6.2	0.1	Rim	3–1	6.2	0.1	Core	3	5.8	0.3	Rim	3–1	6.0	0.1	Core	3	6.5	0.2	Inherited	3a-1	6.5	0.2	Core	3–1	5.4	0.2	Core	3	5.5	0.2	Core
4–1	6.4	0.1	Rim	4–1	6.6	0.1	Rim	4a-1	6.3	0.3	Core	4–1	5.8	0.1	Core	4	6.0	0.2	Inherited	3b	6.1	0.2	Rim	4–1	5.4	0.2	Core	4–1	5.4	0.2	Rim
5	6.0	0.1	Rim	5a-1	6.2	0.1	Rim	4b	6.6	0.3	Rim	5a-1	6.6	0.1	Core	5a	6.2	0.2	Rim	5–1	6.3	0.2	Rim	5	5.3	0.2	Core	5–1	5.3	0.2	Rim
6–1	6.5	0.1	Inherited	5b	6.8	0.1	Core	6	6.0	0.3	Inherited	5b-1	6.2	0.1	Rim	5b	6.5	0.3	Core	6–1	6.4	0.2	Inherited	6	5.2	0.2	Rim	6–1	5.8	0.2	Rim
7–1	6.0	0.1	Rim	7–1	6.4	0.1	Core	7–1	6.2	0.3	Rim	7–1	6.0	0.1	Rim	6a-1	6.8	0.2	Rim	7–1	8.1	0.2	Inherited	7–1	5.2	0.2	Rim	7	5.6	0.2	Rim
8.0	5.7	0.1	Rim	8–1	8.3	0.1	Inherited	8–1	6.4	0.3	Rim	8–1	5.7	0.1	Rim	6b-1	6.3	0.2	Rim	8	7.2	0.2	Inherited	8–1	5.3	0.2	Rim	8–1	5.5	0.2	Core
9.0	5.8	0.1	Core	9–1	6.1	0.1	Core	9	5.9	0.3	Rim	9–1	5.9	0.1	Rim	8	6.2	0.2	Core	9	6.6	0.2	Core	9–1	5.1	0.2	Core	9–1	5.3	0.2	Rim
10.0	5.9	0.1	Rim	10–1	6.1	0.1	Rim	10a	6.1	0.3	Rim	10–1	6.1	0.1	Rim	9–1	6.8	0.2	Rim	10	6.9	0.2	Core	10–1	4.9	0.2	Rim	10–1	5.4	0.2	Rim
11a-1	5.9	0.3	Inherited	11–1	5.9	0.4	Core	11a	7.3	0.3	Inherited	11–1	6.1	0.2	Rim	10a-1	6.8	0.2	Rim	11a	6.9	0.2	Core	11–1	5.1	0.3	Rim	11	5.3	0.3	Rim
11b-1	6.2	0.3	Rim	12–1	6.2	0.4	Rim	11b	5.7	0.3	Rim	12a-1	6.1	0.2	Rim	11–1	6.4	0.3	Rim	11c-1	6.9	0.2	Rim	12–1	5.2	0.3	Core	12–1	5.2	0.3	Rim
13–1	6.0	0.3	Rim	13	6.0	0.4	Core	13–1	5.9	0.3	Rim	12b-1	6.2	0.2	Core	12–1	6.2	0.3	Rim	13a-1	6.2	0.2	Core	13	5.2	0.3	Core	13–1	5.9	0.3	Rim
14–1	6.2	0.3	Inherited	14	6.4	0.4	Rim	14	5.6	0.3	Rim	14a-1	5.8	0.2	Core	14	6.6	0.3	Core	14–1	6.8	0.2	Core	14–1	5.0	0.3	Core	14	5.3	0.3	Rim
15–1	6.2	0.3	Rim	15a-1	7.8	0.4	Inherited	15–1	6.0	0.3	Rim	15	6.6	0.2	Inherited	15	6.0	0.3	Core	15–1	6.0	0.2	Core	15a-1	5.3	0.3	Core	15–1	5.7	0.3	Rim
16–1	6.0	0.3	Rim	15b	6.5	0.4	Rim	16a	7.4	0.3	Inherited	16	6.2	0.2	Rim	16	6.5	0.3	Core	16–1	6.1	0.2	Inherited	16a	5.1	0.3	Core	16	5.7	0.3	Rim
17–1	6.1	0.3	Rim	16–1	6.4	0.4	Rim	16b	6.2	0.3	Rim	17–1	6.0	0.2	Rim	17–1	6.8	0.3	Core	17	6.7	0.2	Core	17	5.2	0.3	Core	17–1	5.5	0.3	Rim
18–1	6.0	0.3	Rim	18a-1	6.6	0.4	Inherited	16c-1	5.9	0.3	Rim	18–1	5.9	0.2	Rim	18a	6.3	0.3	Rim	18–1	6.3	0.2	Rim	18	5.3	0.3	Core	18–1	5.2	0.3	Core
19a-1	5.2	0.3	Inherited	18b	6.5	0.4	Rim	19	5.7	0.3	Core	19–1	5.8	0.2	Rim	18b	5.0	0.3	Inherited	19a	6.2	0.2	Inherited	19a	5.5	0.3	Rim	19–1	6.0	0.3	Rim
19b-1	6.6	0.3	Rim	19–1	6.3	0.4	Core	20a-1	7.3	0.3	Inherited	20–1	6.2	0.2	Core	20	6.5	0.3	Rim	20	6.5	0.2	Rim	20–1	5.6	0.3	Core	20	5.7	0.3	Rim
21–1	6.0	0.2	Rim					20b	7.0	0.2	Rim	21–1	5.9	0.4	Rim									21a-1	5.5	0.2	Core				
22–1	6.3	0.2	Rim					22a	6.1	0.2	Rim	22	6.1	0.4	Inherited									22–1	5.3	0.2	Core				
23–1	6.0	0.2	Rim					22b-1	6.6	0.2	Rim	23a-1	6.0	0.4	Core									23a-1	5.2	0.2	Core				
24.0	6.2	0.2	Rim					24	5.7	0.2	Core	23b	6.4	0.4	Rim									24	5.2	0.2	Core				
25–1	5.9	0.2	Core					25	6.2	0.2	Rim	25a-1	6.1	0.4	Core									25–1	5.4	0.2	Rim				
26–1	6.2	0.2	Core					26–1	6.4	0.2	Rim	25b	6.1	0.4	Rim									26–1	5.2	0.2	Rim				
27.0	6.3	0.2	Core					27–1	6.4	0.2	Rim	27a	5.9	0.4	Rim									27–1	5.4	0.2	Core				
28–1	5.8	0.2	Core					28–1	6.3	0.2	Rim	27b-1	5.9	0.4	Inherited									28	5.3	0.2	Core				
29a	5.5	0.2	Core					29–1	6.5	0.2	Core	29–1	6.5	0.4	Core									29–1	5.2	0.2	Core				
29b-1	5.8	0.2	Rim					30–1	6.3	0.2	Rim	30–1	5.8	0.4	Core									30	5.2	0.2	Core				
								31a-1	6.1	0.3	Core	31	6.3	0.4	Rim																
								31b-1	6.2	0.3	Rim	32	6.5	0.4	Core																
								33–1	5.8	0.3	Rim	33	6.2	0.4	Core																
								34–1	6.4	0.3	Rim	34	5.9	0.4	Core																
								35	6.3	0.3	Core	35a-1	6.3	0.4	Core																
								36a	6.5	0.3	Rim	36a	6.1	0.4	Rim																
								36b-1	7.6	0.3	Inherited	36b-1	6.2	0.4	Core																
								38a	6.5	0.3	Rim	38–1	6.1	0.4	Inherited																
								38b-1	6.1	0.3	Rim	39	6.1	0.4	Core																
								40–1	6.2	0.3	Rim	40–1	6.0	0.4	Core																
Average for core and rim				Average for core and rim				Average for core and rim				Average for core and rim				Average for core and rim				Average for core and rim				Average for core and rim				Average for core and rim			
	6.05	0.48			6.31	0.45			6.18	0.61			6.09	0.41			6.46	0.51			6.53	0.60			5.26	0.31			5.52	0.41	

[a] 'Core' and 'rim' refers to the relative position of the analysis site within the crystal. "Core" means magmatic core, whereas "Inherited" means inherited core.

Table 3
Hafnium isotope ratios of zircons in the Taitao granitoids.

Analysis no.	$^{176}Yb/^{177}Hf$	2 SE		$^{176}Lu/^{177}Hf$	2 SE		$^{176}Hf/^{177}Hf^{*1}$	2 SE		εHf(t)		2 SE*2	Texture	Spot size (μm)
Cabo raper pluton														
TPB56														
3–3	0.027919	±	857	0.000974	±	54	0.282952	±	30	5.61	±	1.08	Rim	40
11b-2	0.024270	±	571	0.000769	±	20	0.282936	±	28	5.05	±	0.98	Rim	40
14–3	0.139821	±	2194	0.003701	±	50	0.282877	±	40	2.96	±	1.41	Inherited core	40
21–3	0.033553	±	471	0.001044	±	14	0.282931	±	28	4.89	±	1.00	Rim	40
22–3	0.042573	±	1265	0.001275	±	46	0.282949	±	26	5.52	±	0.93	Rim	40
23–3	0.026613	±	377	0.000820	±	18	0.282919	±	30	4.47	±	1.07	Rim	40
28–3	0.056546	±	5670	0.001649	±	155	0.283000	±	28	7.33	±	0.99	Magmatic core	40
40	0.033862	±	292	0.001051	±	5	0.282767	±	33	−0.90	±	1.17	Inherited core	40
Average for magmatic core and rim										5.48	±	1.83		
TPE88														
1–3	0.042817	±	1208	0.001323	±	27	0.282917	±	43	4.38	±	1.53	Rim	20
2–3	0.023090	±	1024	0.000822	±	33	0.282997	±	58	7.21	±	2.06	Rim	20
4–3	0.045207	±	2300	0.001345	±	55	0.282940	±	52	5.20	±	1.85	Rim	20
5a-3	0.034957	±	647	0.001109	±	24	0.282951	±	50	5.60	±	1.77	Rim	20
7–3	0.042850	±	3292	0.001256	±	64	0.282885	±	62	3.25	±	2.20	Magmatic core	30
9–2	0.049372	±	3165	0.001513	±	76	0.282989	±	48	6.94	±	1.70	Magmatic core	20
11–3	0.044634	±	1782	0.001349	±	39	0.282927	±	32	4.74	±	1.19	Rim	30
12–3	0.022712	±	1706	0.000716	±	54	0.282915	±	26	4.32	±	0.93	Rim	40
Average for magmatic core and rim										5.20	±	2.51		
TPE90														
4a-3	0.032527	±	262	0.000977	±	8	0.282887	±	70	3.31	±	2.49	Magmatic core	20
22b-2	0.024599	±	152	0.000805	±	17	0.282892	±	25	3.49	±	0.87	Rim	40
27–2	0.026052	±	807	0.000846	±	33	0.282935	±	38	5.01	±	1.34	Rim	20
28–3	0.037532	±	2294	0.001179	±	58	0.282925	±	49	4.66	±	1.74	Rim	20
29–2	0.061163	±	7182	0.001786	±	206	0.282933	±	34	4.97	±	1.20	Magmatic core	40
30–2	0.026160	±	896	0.000825	±	37	0.282936	±	46	5.05	±	1.62	Rim	30
33–3	0.028783	±	1238	0.000898	±	32	0.282863	±	47	2.49	±	1.65	Rim	20
38b-2	0.038411	±	842	0.001215	±	23	0.282894	±	28	3.56	±	0.98	Rim	40
Average for magmatic core and rim										4.07	±	1.83		
Estero Cono Pluton														
TPE135														
1–2	0.061662	±	5384	0.001776	±	159	0.282943	±	25	5.29	±	0.87	Magmatic core	40
3–2	0.089654	±	779	0.002540	±	23	0.282910	±	24	4.12	±	0.84	Magmatic core	40
5b-3	0.061219	±	2189	0.001779	±	61	0.282924	±	28	4.62	±	0.99	Magmatic core	40
12b-2	0.076352	±	2687	0.002257	±	97	0.282949	±	30	5.53	±	1.05	Magmatic core	40
14b-2	0.053258	±	3099	0.001565	±	91	0.282937	±	27	5.09	±	0.97	Magmatic core	40
21–3	0.035461	±	422	0.001037	±	13	0.282947	±	23	5.45	±	0.81	Rim	40
25a-2	0.040933	±	1679	0.001240	±	43	0.282927	±	25	4.75	±	0.87	Rim	40
29–2	0.030930	±	291	0.000952	±	13	0.282929	±	30	4.83	±	1.07	Magmatic core	40
35a-2	0.039589	±	1142	0.001202	±	54	0.282982	±	40	6.69	±	1.42	Magmatic core	40
36b-2	0.095017	±	4445	0.002697	±	127	0.282936	±	27	5.07	±	0.95	Rim	40
38–3	0.066749	±	4375	0.002198	±	201	0.282913	±	31	4.24	±	1.10	Magmatic core	40
40–2	0.061995	±	2123	0.001776	±	50	0.282896	±	28	3.65	±	0.98	Magmatic core	40
Average for magmatic core and rim										4.95	±	1.51		
Bahia barrientos intrusion														
TPB243														
1a-3	0.051471	±	3524	0.001630	±	84	0.283007	±	28	7.58	±	1.00	Magmatic core	40
10b-2	0.049551	±	1250	0.001582	±	24	0.282984	±	35	6.75	±	1.25	Rim	30
Average for magmatic core and rim										7.16	±	0.83		
Tres montes pluton														
TPH75														
2a-2	0.031727	±	229	0.000965	±	29	0.282929	±	30	4.81	±	1.07	Rim	40
3a-2	0.049712	±	1171	0.001427	±	24	0.282870	±	31	2.71	±	1.08	Magmatic core	40
5–3	0.035145	±	1758	0.001043	±	45	0.282886	±	35	3.29	±	1.23	Rim	40
11c-2	0.065974	±	1841	0.001900	±	66	0.282817	±	41	0.86	±	1.43	Rim	20
13a-2	0.084114	±	3351	0.002408	±	86	0.282972	±	34	6.32	±	1.20	Magmatic core	40
14–2	0.112777	±	3150	0.003917	±	99	0.282879	±	64	3.06	±	2.26	Magmatic core	30
Average for magmatic core and rim										3.51	±	3.42		
Seno Hoppner Pluton														
TPG171														
1a-2	0.211101	±	2856	0.005828	±	37	0.282977	±	38	6.51	±	1.35	Magmatic core	40
7–2	0.123086	±	4666	0.003529	±	107	0.283011	±	29	7.70	±	1.02	Rim	40
8–3	0.191111	±	435	0.005196	±	16	0.283032	±	33	8.46	±	1.17	Magmatic core	40
9–3	0.147895	±	1344	0.004127	±	33	0.282980	±	36	6.61	±	1.26	Magmatic core	40
10–2	0.175597	±	2769	0.004858	±	39	0.283005	±	30	7.51	±	1.06	Magmatic core	40
11–3	0.096262	±	5106	0.002719	±	155	0.282982	±	34	6.69	±	1.19	Rim	40
12–3	0.165611	±	3007	0.004625	±	86	0.283052	±	32	9.15	±	1.12	Magmatic core	40

(continued on next page)

Table 3 (*continued*)

Analysis no.	$^{176}Yb/^{177}Hf$	2 SE		$^{176}Lu/^{177}Hf$	2 SE		$^{176}Hf/^{177}Hf$*1	2 SE		εHf(t)		2 SE*2	Texture	Spot size (μm)
14–3	0.139767	±	1108	0.003895	±	28	0.283007	±	30	7.56	±	1.06	Magmatic core	40
15a-2	0.160166	±	6083	0.004391	±	125	0.282999	±	30	7.27	±	1.07	Magmatic core	40
21b	0.179303	±	1203	0.005022	±	16	0.283017	±	37	7.92	±	1.31	Magmatic core	40
22–3	0.153961	±	2429	0.004260	±	72	0.283028	±	29	8.30	±	1.01	Magmatic core	40
23b	0.299838	±	2285	0.007846	±	50	0.282995	±	37	7.15	±	1.31	Magmatic core	40
25–3	0.111076	±	1463	0.003212	±	46	0.283002	±	35	7.38	±	1.25	Rim	40
27–3	0.168620	±	7360	0.004636	±	221	0.282966	±	53	6.11	±	1.88	Magmatic core	40
Average for magmatic core and rim										7.45	±	1.61		
TPD116														
4–3	0.034825	±	615	0.001100	±	23	0.282941	±	47	5.24	±	1.67	Rim	20
6–3	0.047598	±	2792	0.001400	±	65	0.282939	±	51	5.15	±	1.79	Rim	20
8–3	0.023317	±	1068	0.000830	±	35	0.282994	±	57	7.12	±	2.00	Rim	20
Average for rim										5.84	±	1.81		

*1 The $^{176}Hf/^{177}Hf$ ratios are reported relative to 0.282163 in JMC-475 (Blichert-Toft et al., 1997).
*2 Errors in Hf isotopic ratios are 2SE of the mean and include within-run statistics and reproducibility of standard analyses.

4. Results

4.1. Zircon morphology and CL images

Representative CL images of analyzed zircons are shown in Fig. 5. Zircons in the Taitao granitoids typically displayed euhedral shapes with dimensions generally ranging from 50 × 50 to 100 × 200 μm; they are colorless, pink, or orange. Zircons in samples from the Bahia Barrientos intrusion (TPB243), Tres Montes (TPH75), and Seno Hoppner (TPD116) plutons are smaller than those from other plutonic bodies. In general, zircon grains exhibited coherent core-to-rim textures, such as oscillatory zoning (e.g., TPE56–3 and TPB243 in Fig. 5) and/or sector

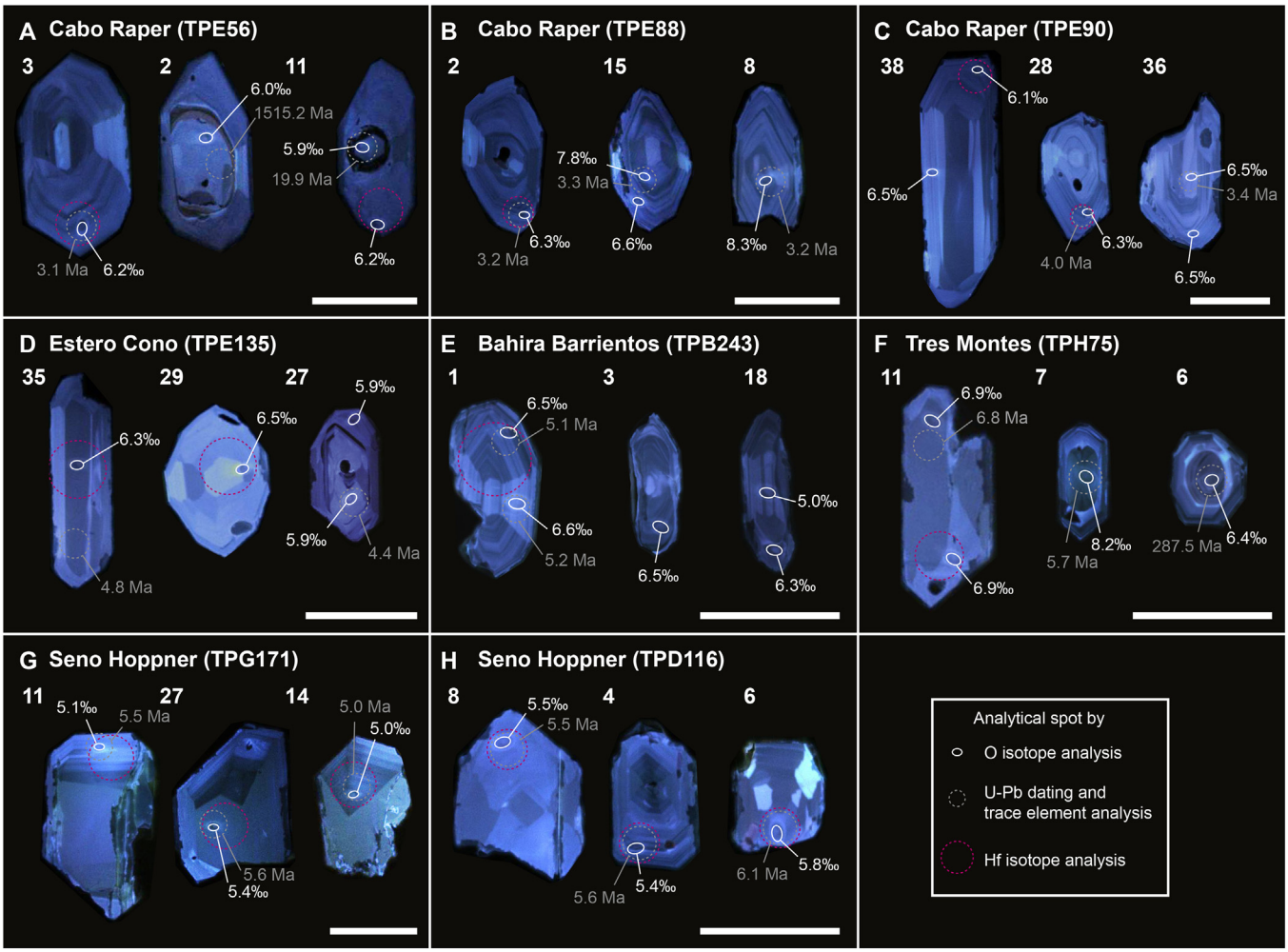

Fig. 5. Cathodoluminescence images of zircons separated from the Taitao granitoids with analytical spots with SIMS and LA-ICP-MS. Zircons from the granitoids show euhedral shapes and display oscillatory zoning and sector zoning. Some zircons include inherited cores (see text for the details). Scale bars are 100 μm.

zoning (e.g., TPG171–14 and TPD116–8 in Fig. 5). On the other hand, some zircon grains show incoherent textures at their cores (e.g., TPE56–2 and TPH75–7 in Fig. 5). Hereafter, we describe the coherent cores in oscillatory zoning or sector zoning as "magmatic core" and the incoherent cores as "inherited core" (Tables 1–3).

Inherited cores are observed in the zircons from granitoids in the Cabo Raper, Estero Cono, Tres Montes plutons and the Bahia Barrientos intrusion (Figs. 5A–F). The Tres Montes pluton had the highest percentage of zircons, including inherited cores, among the Taitao granitoids (Fig. 5F). This observation is consistent with that of Anma et al. (2009). The optical nature of the inherited cores differed depending on the sample. Specifically, inherited cores in TPH75–6 and TPB243–18 showed as pale violet in CL images, whereas their surrounding rims showed as light blue (Figs. 5E and F). The brightness of inherited cores in zircons from TPE56–11 was darker than that of their rims (Fig. 5A). On the other hand, the differences in color and brightness between inherited cores and their rims in some zircons separated from TPE88, TPE90, and TPE135 (for example, TPE88–15, TPE88–8, and TPE90–36; Figs. 5B and C) are obscure.

Zircons in the microtrondhjemite dike (TPG171) from the Seno Hoppner pluton displayed a large homogeneous zone, which formed an angular shape, within their core (Fig. 5G). These cores are mantled by rims showing fine oscillatory zoning. On the other hand, such large homogeneous cores are rare in zircon grains from another trondhjemite from the Seno Hoppner pluton (TPD116). Instead, most grains displayed fine oscillatory zoning from core to rim (Fig. 5H). We considered both of these cores as magmatic cores.

4.2. REE composition and U—Pb age

The REE compositions of the zircons are shown in Table S3, and CI chondrite-normalized REE patterns are shown in Fig. S2. All zircons displayed HREE-enriched patterns, which are common in igneous zircon (e.g., Hoskin and Ireland, 2000). Almost all zircons displayed a positive Ce anomaly and negative Eu anomaly, the latter reflecting the degree of fractional crystallization of plagioclase before zircon formation (e.g., Hoskin and Schaltegger, 2003). In REE concentrations, no significant variations are observed between magmatic core, rim, and inherited core (Fig. S2). The observed variation in zircon Yb/Sm ratio for the Seno Hoppner pluton is relatively small, compared with those for the Cabo Raper pluton and Bahia Barrientos intrusion (Table S3).

The U—Pb ages of zircons are shown in Table 1. The Th/U ratios of most zircons fall within the range of typical Th/U ratios of igneous zircons (> 0.5; Hoskin and Schaltegger, 2003). The obtained ^{238}U—^{206}Pb ages from magmatic cores and rims in zircons from the Cabo Raper (4.1 ± 1.2 Ma), Estero Cono (5.1 ± 0.7 Ma), Tres Montes (5.5 ± 1.3 Ma), and Seno Hoppner plutons (5.3 ± 0.9 Ma) and the Bahia Barrientos intrusion (4.9 ± 0.7 Ma) are similar to those reported in previous work (3.84–5.70 Ma; Anma et al., 2006). The ages of inherited cores in the zircons from the Cabo Raper and Tres Montes plutons varied from 3.2 to 1515.2 Ma (Fig. 5 and Table 1). On the other hand, the ages of inherited cores in the zircons from the Estero Cono pluton ranged from 4.4 to 5.6 Ma, which is similar to those of their surrounding rims and magmatic cores.

4.3. O isotope ratios of zircons

The O isotope compositions of the zircons are shown in Table 2 and Fig. 6. The $\delta^{18}O_{Zrc}$ values of magmatic cores and rims in the zircons ranged from 4.9‰ to 6.9‰, with mean values of the individual plutons as follows (Fig. 6): Tres Montes (6.53 ± 0.60‰, 2SD), Bahia Barrientos (6.46 ± 0.51‰), Cabo Raper (6.17 ± 0.54‰), Estero Cono (6.09 ± 0.41‰), and Seno Hoppner (5.37 ± 0.44‰). Almost all $\delta^{18}O_{Zrc}$ values from the Seno Hoppner pluton are identical to those of mantle-equilibrated zircons (5.3‰ ± 0.6‰; Valley et al., 1998) within analytical uncertainty, whereas most zircons from the other four plutons exhibited ca. 1‰ higher $\delta^{18}O_{Zrc}$ values compared with mantle-equilibrated zircons.

Except for the Seno Hoppner pluton, inherited cores are observed in zircons from four plutonic bodies (Fig. 5). The $\delta^{18}O$ values in the inherited cores ranged from 5.0‰ to 8.3‰ (Table 2). The distribution patterns of the $\delta^{18}O$ values varied between the four plutons (Fig. 6). The Tres Montes and Capo Raper plutons included inherited cores exhibiting higher $\delta^{18}O$ values (7.22–8.32‰) than those of their magmatic cores and rims. Single inherited cores in both the Bahia Barrientos intrusion and Capo Raper pluton showed mantle-like $\delta^{18}O$ values (4.99‰ and 5.19‰, respectively), which are lower than those of their magmatic cores and rims. In contrast, the range of $\delta^{18}O$ values for inherited cores in zircons from the Estero Cono pluton is equivalent to that from their magmatic cores and rims (Fig. 6).

4.4. Zircon Hf isotope ratio

The measured zircon Hf isotope ratios are listed in Table 3. They are also plotted as a function of $\delta^{18}O$ value in Fig. 7, together with the results of whole-rock analyses. Data from inherited cores are not included in Fig. 7. The εHf(t) values of all zircons from the Taitao granitoids ranged from 0.86 to 9.15. The observed zircon Hf isotopic values are negatively correlated with the zircon $\delta^{18}O$ values, and these data sets are distributed between those of the sedimentary rocks and dolerite-gabbro-pyroxenite in the Taitao ophiolite. The microtrondhjemite (TPG171) in the Seno Hoppner pluton, which included zircons exhibiting mantle-like $\delta^{18}O$ values, exhibited higher zircon εHf(t) values (7.45 ± 1.61), compared with other granitoids that include zircons having elevated $\delta^{18}O$ values (from 3.51 to 7.16; Table 3). The εHf(t) values of all zircons from the Seno Hoppner pluton are within the range of mid-ocean ridge basalts reported by Andres et al. (2004) (from 3.47 to 23.16; these values were recalculated by using the chondritic parameters of Iizuka et al. (2015)).

4.5. Whole-rock O isotope ratios

Whole-rock major element composition is shown in Table 4 and Table S5 and Fig. 4. The results of whole-rock O isotopic analysis on 11 samples that were exposed around the Taitao granitoids are shown in Table 4. The $\delta^{18}O_{WR}$ values of the sedimentary rocks (8.32–10.70‰), altered basalts (8.00–8.34‰), and gabbro (6.11‰) within the ophiolite, and the sedimentary rocks in the basement (7.91–11.29‰) are elevated compared with the mantle values (5.4–5.8‰; Ionov et al., 1994). On the other hand, the dolerite and pyroxenite within the ophiolite showed lower $\delta^{18}O_{WR}$ values (4.40‰ and 4.85‰, respectively) compared with the mantle values.

4.6. Whole-rock Hf isotope ratios

The results of whole-rock Hf isotope analysis are shown in Table 4. The pyroxenite in the ophiolite showed the highest εHf value (19.10 ± 0.27). The εHf values of the gabbro (15.02 ± 0.51), dolerite (13.73 ± 0.41), and altered basalts (9.78–12.82) are also within the range of juvenile continental crust (Iizuka et al., 2017). Except for one of the altered basalts (TPH 342), these εHf values are similar to those of N-MORB (12.9–23.9; Andres et al., 2004). On the other hand, the εHf values from the sedimentary rocks within the ophiolite body (−7.10 to 1.25) and the sedimentary rocks in the basement (−1.44 to 0.47) are clearly lower than those of mafic–ultramafic rocks.

5. Discussion

5.1. Protoliths of the Taitao granitoids

The combination of $\delta^{18}O_{Zrc}$ and Hf isotope ratios for zircon enabled us to estimate the magmatic protolith (e.g., Kemp et al., 2007; Li et al.,

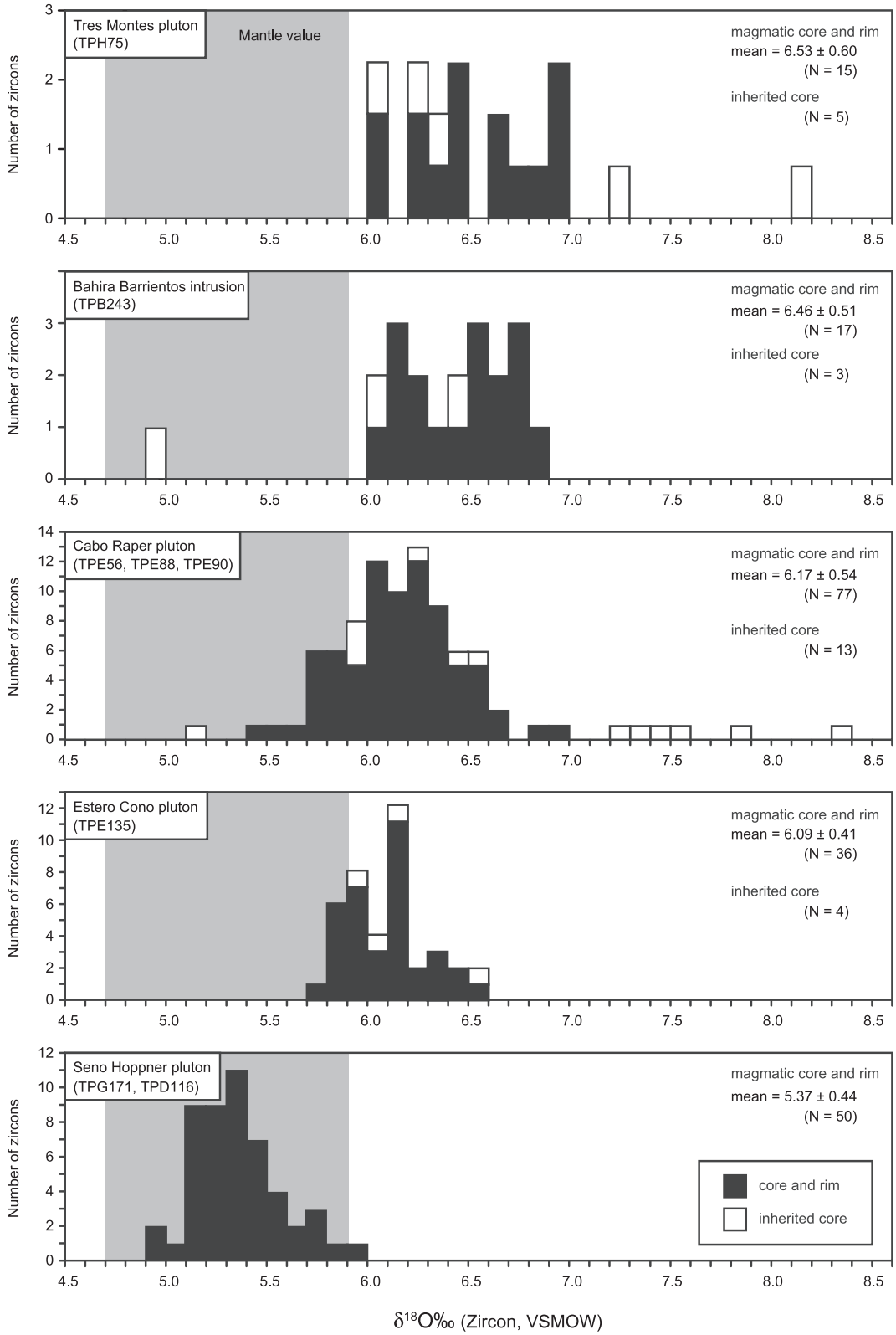

Fig. 6. Frequency diagrams of O isotope ratios in zircons. Data for the magmatic cores and rims are represented by black squares, whereas data from inherited cores are expressed as open symbols. Gray area corresponds to the range of O isotope values of mantle, as deduced from zircons in kimberlite (Valley et al., 1998).

2010). The $\delta^{18}O_{Zrc}$ value is nearly constant during the crystal fractionation process (Lackey et al., 2008; Valley et al., 1994), and the $\delta^{18}O$ value of non-metamict zircon is resistant to later alteration by meteoric water (e.g., Cherniak and Watson, 2003; Page et al., 2007a), contrary to the $\delta^{18}O_{WR}$ value (e.g., Eiler, 2001; Eiler et al., 2000; Ito et al., 2003; Lackey et al., 2008; Matsuhisa, 1979; Taylor Jr and Sheppard, 1986). For this reason, the $\delta^{18}O_{Zrc}$ value is more suitable than the $\delta^{18}O_{WR}$ value for estimating the protolith of granitoids. Because the zircons in

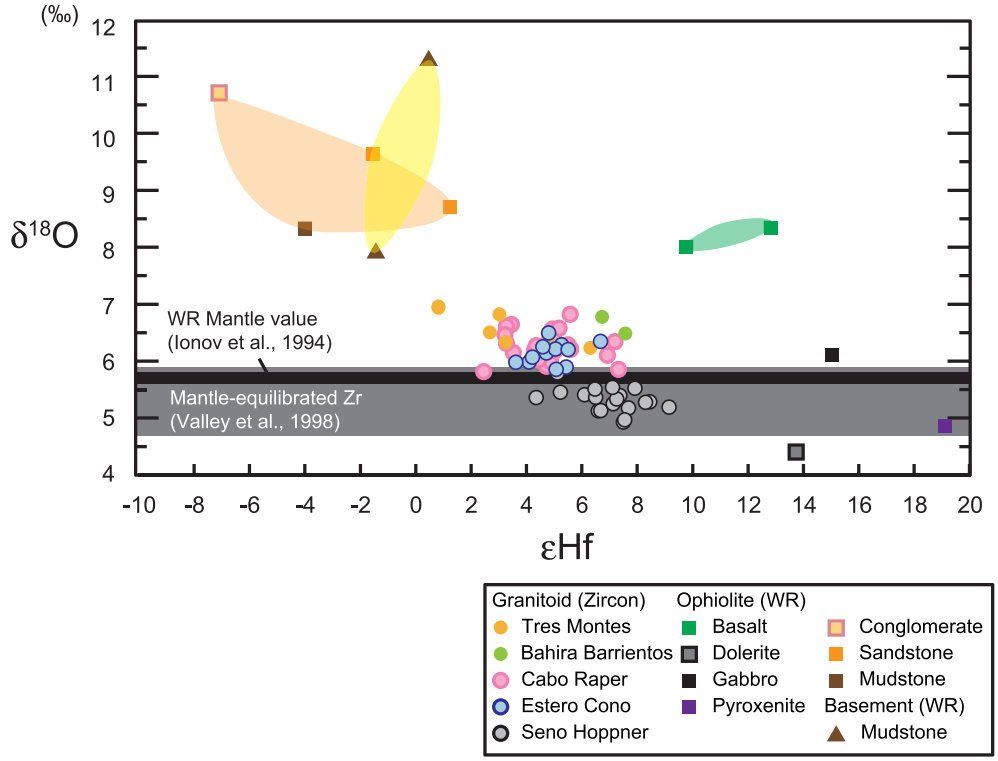

Fig. 7. Whole-rock and zircon Hf–O diagram. The Hf–O isotope ratios of zircons of the Taitao granitoids are shown as filled circles. Values of $\delta^{18}O$ (whole rock) in the Taitao ophiolite and the pre-Jurassic basement rocks are shown as filled squares and filled triangles, respectively. Mantle values from whole rocks (Ionov et al., 1994) and zircons (Valley et al., 1998) are also shown as black and gray bars, respectively. WR: whole rock, Zr: zircon.

Table 4
Major element compositions and Hf–O isotope ratios for the Taitao Ophiolite, sediment and basement rocks.

Unit	Taitao Ophiolite					Sediment				Basement	
	MVU										
Sample No.	TPH 347	TPH 342	TPE 110	TPE 73	TPE 30	TPB 252	TPB 298	TPH 317	TPH 314	TPE 392	TPD 97
Rock	Basalt	Basalt	Dolerite	Gabbro	Pyroxenite	Mudstone	Sandstone	Sandstone	Conglomerate	Mudstone	Mudstone
SiO_2 (wt%)	54.75	54.82	52.19	47.13	51.39	73.32	63.70	62.82	67.55	62.84	67.98
TiO_2 (wt%)	1.38	1.09	1.60	0.24	0.12	0.51	0.84	0.77	0.58	0.83	0.80
Al_2O_3 (wt%)	14.11	17.49	14.86	18.15	4.67	13.03	16.35	16.04	14.17	17.79	15.78
Fe_2O_3 (wt%)	8.86	7.93	10.30	8.94	3.21	3.95	6.13	6.62	4.81	6.88	5.57
MnO (wt%)	0.16	0.13	0.16	0.12	0.03	0.06	0.06	0.09	0.08	0.10	0.08
MgO (wt%)	5.00	5.00	6.26	13.86	19.61	1.62	2.77	3.54	2.07	2.65	2.10
CaO (wt%)	9.28	7.39	9.39	9.10	19.28	2.41	3.88	2.57	4.07	2.27	0.86
Na_2O (wt%)	5.23	4.62	4.11	2.17	0.41	3.40	3.41	3.68	3.19	3.07	2.76
K_2O (wt%)	0.34	0.83	0.46	0.03	b.d.l*1	1.06	2.29	3.15	2.54	3.13	3.14
P_2O_5 (wt%)	0.08	0.08	0.10	b.d.l*1	b.d.l*1	0.04	0.09	0.07	0.07	0.10	0.09
Total (wt%)	99.20	99.39	99.43	99.76	98.72	99.40	99.52	99.34	99.12	99.67	99.14
K_2O/Na_2O	0.07	0.18	0.11	0.01	b.d.l*1						
$K_2O + Na_2O$	5.57	5.44	4.56	2.21	0.41						
ASI*2	0.55	0.80	0.61	0.90	0.13						
$\delta^{18}O \pm 2$ SD (‰)	8.34 ± 0.12	8.00 ± 0.12	4.40 ± 0.12	6.11 ± 0.12	4.85 ± 0.12	8.32 ± 0.12	9.63 ± 0.12	8.70 ± 0.12	10.70 ± 0.12	7.91 ± 0.12	11.29 ± 0.12
$^{176}Yb/^{177}Hf$	#######	#######	#######	#######	#######	#######	b.d.l.	b.d.l.	0.000001	b.d.l.	0.000012
$^{176}Lu/^{177}Hf$*3	#######	b.d.l.	b.d.l.	b.d.l.	#######	b.d.l.	b.d.l.	b.d.l.	b.d.l.	b.d.l.	0.000001
$^{176}Hf/^{177}Hf$	0.283155	0.283070	0.283181	0.283218	0.283333	0.282680	0.282749	0.282828	0.282592	0.282752	0.282806
2 SE*4	0.000007	0.000007	0.000012	0.000014	0.000008	0.000013	0.000014	0.000011	0.000010	0.000011	0.000011
εHf	12.82	9.78	13.73	15.02	19.10	−4.00	−1.55	1.25	−7.10	−1.44	0.47
2 SE*4	0.23	0.23	0.41	0.51	0.27	0.45	0.51	0.40	0.36	0.37	0.39

*1 b.d.l. means below detection limit.
*2 ASI means aluminum index.
*3 The $^{176}Hf/^{177}Hf$ ratios are reported relative to 0.282160 in JMC-475 (Blichert-Toft et al., 1997).
*4 Errors in Hf isotopic ratios are 2SE of the mean and include within-run statistics and reproducibility of standard analyses.

the Taitao granitoids are young (ca. 4–6 Ma; Table 1) and not metamict (Fig. 5), the influence of later alteration processes on the $\delta^{18}O_{Zrc}$ and εHf (t) values was likely minor (Valley et al., 2015; Wang et al., 2014). Moreover, we determined the $\delta^{18}O_{WR}$ and whole-rock εHf values of possible protoliths of the Taitao granitoids. Because Hf is fluid-immobile, the whole-rock Hf isotope ratio would not have been significantly changed by later alteration processes. On the other hand, the $\delta^{18}O_{WR}$ value is more labile than the Hf isotope ratio. The sequence of the Taitao ophiolite serves as a record of seafloor metamorphism (Shibuya et al., 2007). The petrological study indicates that dehydration during emplacement of the Taitao ophiolite was likely minor, implying that the $\delta^{18}O_{WR}$ values in the rocks did not change significantly at this time. Because reaction between rocks and meteoric water at the surface decreased the whole-rock O isotope ratio, the $\delta^{18}O_{WR}$ values in this study are regarded as the lower limit of the O isotope ratios of the whole-rock samples.

The $\delta^{18}O_{Zrc}$ values from the Tres Montes, Cabo Raper, Bahia Barrientos, and Estero Cono plutons are identical to, or slightly higher than, those of mantle-equilibrated zircons (5.3 ± 0.6‰; Valley et al., 1998, 2005; Page et al., 2007b; Table 2, Fig. 6). Among the rocks surrounding the Taitao granitoids, sedimentary rocks (from 7.9 to 11.3‰) and altered basalts (from 8.0 to 8.3‰) showed elevated $\delta^{18}O_{WR}$ values (Table 4). Therefore, the slightly elevated $\delta^{18}O_{Zrc}$ values of these four plutons suggest the involvement of (i) sedimentary rocks and/or (ii) altered basalts in the generation of the granitoid magma. The εHf (t) values of zircons from the Taitao granitoids are negatively correlated with the $\delta^{18}O_{Zrc}$ values (Fig. 7). This distribution pattern is better explained on the basis of mixing with the sedimentary rocks than with the altered basalts, thereby suggesting the contribution of sedimentary rocks to some of the Taitao granitoids. This view is consistent with the previous works which have noted the contamination of the granitoid magma by sedimentary rocks based on Nd—Sr isotope ratios (Kaeding et al., 1990; Shin et al., 2015). Anma and Orihashi (2013) suggested that igneous rocks including Taitao granitoids show evidence for incorporation of subducted sediments rather than sediment within the basement, based on age distribution of detrital and xenocrystic zircons. Because subducting oceanic crust was young, volume of pelagic sediment on the crust was likely much smaller than that of trench-fill sediment. Thus, we consider that the trench-fill sediment accounted for a large portion of the assimilated sediments.

Inherited cores, viewed by CL, are found in zircons from the Tres Montes, Bahia Barrientos, Cabo Raper, and Estero Cono plutons (Fig. 5). The $\delta^{18}O$ values of the inherited cores of zircons range from 5.0 to 8.3‰, some of which are higher than the $\delta^{18}O$ range of the magmatic core and rim (Table 2; Fig. 6). In addition, the U—Pb ages of the inherited cores are up to ~1500 m.y. older than those of the magmatic core and rim (Table 1). These data also suggest assimilation of zircons from sedimentary rocks during formation of the four plutons. The magmatic core and rim of zircons from the Tres Montes pluton showed the highest mean $\delta^{18}O$ value (6.53 ± 0.60‰; Figs. 6 and 7) and the lowest mean εHf(t) value (3.51 ± 3.42; Table 3 and Fig. 7) among the five analyzed plutons. Inherited zircons are found most frequently in the Tres Montes pluton (Fig. 6), as reported in previous studies (Anma et al., 2009; Shin et al., 2015). The mosaic texture observed in the Tres Montes pluton (Fig. 3D) also suggests contamination by the sedimentary rocks such as TPB252. These lines of evidence suggest that the parental magma of the Tres Montes pluton was contaminated by sedimentary rocks more significantly than those of the other plutons. The result is consistent with the Sr—Nd isotope ratios of the Tres Montes pluton (Shin et al., 2015). The nature of CL images of the inherited core differed depending on the sample (Fig. 5). This difference may result from variation in the source rock of the zircon and/or variation in the melting temperature when the inherited zircons were included.

Unlike the other plutons, almost all $\delta^{18}O_{Zrc}$ values from the Seno Hoppner pluton are identical to those of the mantle-equilibrated zircon (Figs. 6 and 7; Valley et al., 1998, 2005; Page et al., 2007b). In addition, all εHf(t) values of zircons in the Seno Hoppner pluton are within the range of mid-ocean ridge basalts (3.47–23.16; Andres et al., 2004). Taking into consideration the fact that inherited cores are not observed in zircons from the Seno Hoppner pluton (Fig. 5), it is considered that the parental magma of the Seno Hoppner pluton involved minor sedimentary rocks during emplacement and that its Hf—O isotope ratios were little influenced by sedimentary rocks. Based on the minor amount of inherited zircon, previous studies have also suggested that the Seno Hoppner and Cabo Raper plutons were formed from rather juvenile granitoid magma (Anma et al., 2009; Kon et al., 2013). The Sr—Nd isotopic data in previous studies suggested minor (5–10%) contamination of sedimentary rocks in the Seno Hoppner pluton compared with other plutons (~10–30%; Kaeding et al., 1990; Shin et al., 2015). Smaller variation in zircon Yb/Sm ratio for the Seno Hoppner pluton than those for the Cabo Raper pluton and Bahia Barrientos intrusion (Table S3) also supports the minor contamination of sedimentary rocks in the Seno Hoppner pluton. These results imply that juvenile granitoid magmas generated by slab-melting have Hf and O isotope compositions similar to those of the upper mantle.

5.2. Implications for slab-melting components

The O and Hf isotopic data for the Taitao granitoids, Taitao ophiolite, and sedimentary rocks in the pre-Jurassic basement indicate that the Taitao granitoids were generated by the mixing of juvenile components that had higher εHf values and sedimentary components that had elevated $\delta^{18}O$ and lower εHf values (Fig. 7). There are two candidates for the juvenile component: partial melting of (i) a parent rock that had a mantle-like $\delta^{18}O$ value and/or (ii) several types of rocks, at least one of which had a lower $\delta^{18}O$ value. Based on the geological setting (Fig. 2), the most plausible candidate for the juvenile component of the Taitao granitoids is subducted oceanic crust. Oceanic crust formed in an oceanic environment commonly suffers seafloor metamorphism, and O isotope ratios of rocks in the oceanic crust are overprinted depending on the reaction temperature, from higher $\delta^{18}O$ values at the surface to lower $\delta^{18}O$ values in deeper portions of the crust (e.g., Gregory and Taylor, 1981). Indeed, within the Taitao ophiolite, altered basalts exhibited higher $\delta^{18}O_{WR}$ values (up to 8.34‰), and dolerite had a lower $\delta^{18}O_{WR}$ value (4.40‰; Table 4 and Fig. 7) compared with the mantle $\delta^{18}O$ value. In general, because the water content of oceanic crust decreases from surface basalt to deeper gabbro, basalt should be more readily melted than gabbro in subducted oceanic crust. Therefore, it is unlikely that the mantle-like $\delta^{18}O_{Zrc}$ values of the Taitao granitoids resulted solely from partial melting of a parent rock that had a mantle-like $\delta^{18}O$ value. Rather, we argue that the slab-melting generated in the Taitao granitoids extended from surface basalt with a higher $\delta^{18}O_{WR}$ value to deeper dolerite with a lower $\delta^{18}O_{WR}$ value (Fig. 8), resulting in the generation of granitoid magma with a mantle-like O isotope signature (Fig. 7). Therefore, partial melting of (ii) several types of rocks, at least one of which had a lower $\delta^{18}O$ value (in this case, dolerite), is the most likely process to create the juvenile component. Thermodynamic calculations have indicated that the dolerite, including TPE110, was at ca. 2–4 km depth in the oceanic crust (Shibuya et al., 2007). Thus, the Taitao granitoids would have been generated by partial melting of at least the upper half of the subducted oceanic crust.

The melting depth of the subducted oceanic crust was estimated numerically in a previous study. Iwamori (2000) calculated the temperature and H_2O distributions of subducted oceanic crust to constrain the timing of melting and metamorphism in such a subducted oceanic and the overlying arc crust. In a case where the subduction velocity is 6.3 cm/yr, melting could occur when young (−2.5 to 10 m.y. relative to the timing of ridge subduction) oceanic crust subducts. This subduction velocity and timing of melting could be similar to those of the formation process of the Taitao granitoids. This calculation further suggests that melting of the uppermost and the lowermost parts in the subducted oceanic crust could occur in 0.5 m.y. However, Iwamori

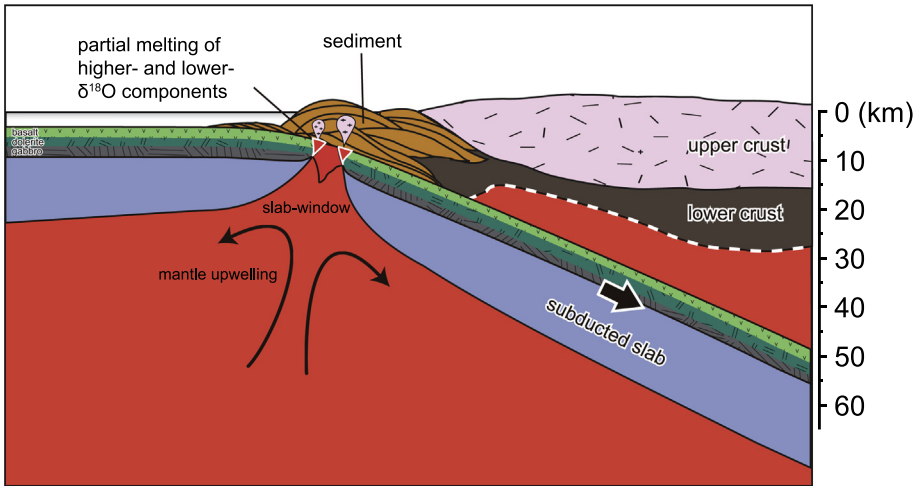

Fig. 8. Schematic model showing the formation of the Taitao granitoids (modified after Kon, 2009). Partial melting of the upper half of oceanic crust involves altered basalt (higher $\delta^{18}O$ and higher εHf component) and dolerite (lower $\delta^{18}O$ and higher εHf component) sequences, generating juvenile granitoid magma with a mantle-like $\delta^{18}O$ value. The granitoid magma that intrudes into sedimentary rocks (higher $\delta^{18}O$ and lower εHf component) creates mixing between the surrounding sedimentary rocks and the juvenile granitoid magma (Fig. 7).

(2000) assumed that 7-km thick subducted oceanic crust homogenously contained 6 wt% H_2O, initially. If the water content decreased with depth, as seen in modern oceanic crust (e.g., Ito and Clayton, 1983; Stakes and O'Neil, 1982), the melting of the lowermost part in the subducted oceanic crust would be inhibited in practice. In this regard, the prediction based on numerical modeling is consistent with our suggestion that the melting of the upper half of the subducted oceanic crust occurs beneath the Taitao peninsula (Fig. 8).

5.3. Implications for Archean granitoids

The major formation process of the Archean granitoids is considered to be different from that of the post-Archean granitoids. Slab-melting at depth of garnet stability field is the most plausible process to account for the chemical compositions of the Archean TTGs (Martin, 1986, 1999). In this case, most slab-melts would have ascended through the mantle after generation, and they should have interacted with the surrounding mantle to some extent. This interaction might have caused an exchange of oxygen isotopes between the TTG melts and the mantle peridotite (Bindeman et al., 2005) and modified the initial O isotopic value of the TTG melt. TTG melts that highly reacted with mantle peridotite would become melts having the composition of the sanukitoid series (Martin et al., 2009) or adakite. If the initial TTG melts reacted with mantle peridotite sufficiently to equilibrate O isotope ratio, the composition of the reacted melt would have likely become markedly different from that of TTG. In turn, the $\delta^{18}O_{Zrc}$ value of TTG formed by the slab-melting process is nearly unchanged during magma ascent, and it would preserve the O isotope ratio of the initial TTG melt.

Some previous works have reported $\delta^{18}O_{Zrc}$ values of Archean granitoids (e.g., King et al., 1998; Valley et al., 2005; Van Kranendonk et al., 2015). The $\delta^{18}O_{Zrc}$ values of TTG with ages of 2670–2740 Ma in the Superior Province range from 4.67 to 6.28‰, with an average value of 5.48 ± 0.78‰ (2 SD) (King et al., 1998). King et al. (1998) suggested that recycling of high $\delta^{18}O$ sources, such as sedimentary and supracrustal rocks, was not predominant in the main crustal growth events of the Superior Province. The $\delta^{18}O_{Zrc}$ values of monzogranites in the Pilbara Craton, whose ages are 3030–3090 Ma, range from 4.87 to 7.07‰, with an average value of 6.2 ± 1.3‰ (Van Kranendonk et al., 2015). Valley et al. (2005) indicated that none of Archean magmatic zircon have $\delta^{18}O$ values higher than 7.5‰. The Archean O isotopic variation is narrower than those observed in Proterozoic granitoids in the Grenville Province (6.80–13.51‰; Valley et al., 1994; Peck et al., 2004) and Phanerozoic granitoids in the Sierra Nevada Batholith (4.21–8.70‰; Lackey et al., 2008). The $\delta^{18}O_{Zrc}$ values of the Seno Hoppner pluton (5.37 ± 0.44‰, Fig. 6) are similar to those of TTGs reported by King et al. (1998), which offers further insight into the mechanism of Archean granitoid genesis. In view of the above discussion, the mantle-like $\delta^{18}O_{Zrc}$ values of the Archean granitoids (e.g., King et al., 1998; Valley et al., 2005) may reflect melting of at least the altered dolerite sequence, if these granitoids were formed by melting of the subducted slab. This is because the involvement of altered basalt and cover sediments increases the $\delta^{18}O$ value of parent granitoid magma. From this perspective, partial melting of subducted oceanic slab reached the upper half during the Archean, although this model is valid only if we assume that the Archean granitoid was generated by slab-melting processes and that the suite of O isotope ratios within the subducted oceanic crust was similar to the modern equivalent (e.g., Gregory and Taylor, 1981; this study).

6. Conclusion

We analyzed the O isotope ratios of 220 spots and Hf isotope ratios of 61 spots on zircons separated from eight granitoids of five plutons in the Taitao Peninsula (the Cabo Raper, Seno Hoppner, Estero Cono, Bahia Barrientos, and Tres Montes plutons). We further measured Hf—O isotope ratios of 11 whole-rock samples from the ophiolite body (basalts, dolerite, gabbro, pyroxenite, mudstone, sandstones, and conglomerate) and basement rocks (mudstones), which are intruded by the granitoids.

The $\delta^{18}O_{Zrc}$ values of the granitoids are negatively correlated with the zircon εHf(t) values, and the Hf and O isotopic data sets of sedimentary rocks around the granitoids are an extension of the correlation curve. The εHf(t) values of the zircons from the Seno Hoppner pluton are within the range of mid-ocean ridge basalts. Therefore, this distribution pattern in the Hf—O isotopic cross-plot can be explained by partial melting of juvenile oceanic crust and involvement of sedimentary rocks. The $\delta^{18}O_{Zrc}$ values of the Seno Hoppner pluton (5.37 ± 0.44‰) are identical to those of mantle-equilibrated zircons, whereas those of the other four plutons are relatively high (6.09–6.53‰). The latter finding indicates that the four plutons included more sedimentary rocks as their parent rocks during their magma emplacements (compared with the Seno Hoppner pluton), which is consistent with the microscopic observations and age frequency distribution of U—Pb ages of the inherited zircons in this study. Our data indicate that in terms of Hf and O isotope ratios, juvenile granitoid magmas generated by slab-melting have compositions similar to those of the upper oceanic crust, if the granitoids involved few sedimentary rocks as their source rocks. To account for the

mantle-like $\delta^{18}O_{Zrc}$ values of the Seno Hoppner pluton, it is necessary that partial melting of the oceanic crust reached the altered dolerite sequence.

Supplementary data to this article can be found online at https://doi.org/10.1016/j.lithos.2020.105665.

Declaration of Competing Interest

The authors declare that they have no known competing financial interest of personal relationships that could have appeared to influence the work reported in this paprt.

Acknowledgments

We are grateful to Prof.Victor A. Ramos and an anonymous reviewer for their helpful comments and constructive suggestions, and the Editor Xian-Hua Li for the handling of this manuscript. We are grateful to Prof. S, Maruyama for financial support during the geological survey in the Taitao area and helpful discussion. We are grateful to John Valley, Noriko Kita and Jim Kern for helpful discussions and kind support in SIMS oxygen isotope analysis at the University of Wisconsin-Madison. Prof. John W. Valley reviewed an early draft of this paper. Mike Spicuzza assisted in laser fluorination analysis of oxygen isotope ratios at UW-Madison. The WiscSIMS ion microprobe laboratory is supported by National Science Foundation (EAR-1658823) and the University of Wisconsin – Madison. KS appreciates Prof. K. Ozawa for helpful comment for the observation of the petrography. We would like to thank Enago (www.enago.jp) for the English language review. This work was supported by grants for JSPS KAKENHI Grant Number 14 J12001.

References

Andres, M., Blichert-Toft, J., Schilling, J.G., 2004. Nature of the depleted upper mantle beneath the Atlantic: evidence from Hf isotopes in normal mid-ocean ridge basalts from 79 N to 55 S. Earth Planet. Sci. Lett. 225, 89–103.

Anma, R., Orihashi, Y., 2013. Shallow-depth melt eduction due to ridge subduction: LA-ICPMS U-Pb igneous and detrital zircon ages from the Chile Triple Junction and the Taitao Peninsula, Chilean Patagonia. Geochem. J. 47, 149–165.

Anma, R., Armstrong, R., Danhara, T., Orihashi, Y., Iwano, H., 2006. Zircon sensitive high mass-resolution ion microprobe U-Pb and fission-track ages for gabbros and sheeted dykes of the Taitao ophiolite, Southern Chile, and their tectonic implications. Island Arc 15, 130–142.

Anma, R., Armstrong, R., Orihashi, Y., Ike, S.I., Shin, K.C., Kon, Y., Komiya, T., Ota, T., Kagoshima, S., Shibuya, T., Yamamoto, S., Veloso, E.E., Fanning, M., Hervé, F., 2009. Are the Taitao granites formed due to subduction of the Chile ridge? Lithos 113, 246–258.

Bangs, N., Cande, S.C., Lewis, S.D., Miller, J.J., 1992. Structural framework of the Chile margin at the Chile Ridge collision zone. Proceedings of the Ocean Drilling Program, Initial Reports. 141, pp. 11–21.

Barker, F., 1979. Trondhjemite: definition, environment and hypotheses of origin. Developments in Petrology. 6. Elsevier, pp. 1–12.

Behrmann, J.H., Lewis, S.D., Cande, S.C., 1994. Tectonics and geology of spreading ridge subduction at the Chile Triple Junction: a synthesis of results from Leg 141 of the Ocean Drilling Program. Geol. Rundsch. 83, 832–852.

Bindeman, I.N., Eiler, J.M., Yogodzinski, G.M., Tatsumi, Y., Stern, C.R., Grove, T.L., Portnyagin, M., Hoernle, K., Danyushevsky, L.V., 2005. Oxygen isotope evidence for slab melting in modern and ancient subduction zones. Earth Planet. Sci. Lett. 235, 480–496.

Blichert-Toft, J., Chauvel, C., Albarède, F., 1997. Separation of Hf and Lu for high-precision isotope analysis of rock samples by magnetic sector-multiple collector ICP-MS. Contrib. Mineral. Petrol. 127, 248–260.

Bourgois, J., Lagabrielle, Y., Le Moigne, J., Urbina, O., Janin, M.C., Beuzart, P., 1993. Preliminary results of a field study of the Taitao ophiolite (southern Chile): implications for the evolution of the Chile triple junction. Ofioliti 18, 113–129.

Bourgois, J., Martin, H., Lagabrielle, Y., Le Moigne, J., Jara, J.F., 1996. Subduction erosion related to spreading-ridge subduction: Taitao peninsula (Chile margin triple junction area). Geology 24, 723–726.

Bourgois, J., Lagabrielle, Y., Martin, H., Dyment, J., Frutos, J., Cisternas, M.E., 2016. A review on forearc ophiolite obduction, adakite-like generation, and slab window development at the Chile triple junction area: uniformitarian framework for spreading-ridge subduction. Pure Appl. Geophys. 173, 3217–3246.

Cahill, T., Isacks, B.L., 1992. Seismicity and shape of the subducted Nazca plate. J. Geophys. Res. 97, 17503–17529.

Cande, S.C., Leslie, R.B., 1986. Late Cenozoic tectonics of the southern Chile trench. J. Geophys. Res. Solid Earth 91 (1978–2012), 471–496.

Cherniak, D.J., Watson, E.B., 2003. Diffusion in zircon. Rev. Mineral. Geochem. 53, 113–143.

Couch, R., Whitsett, R., Hehn, B., Bricerno-Guarupe, L., 1981. Structures of the continental margin of Peru and Chile. Geol. Soc. America Memoir 154, 703–726.

Defant, M.J., Drummond, M.S., 1990. Derivation of some modern arc magmas by melting of young subducted lithosphere. Nature 347, 662–665.

Eiler, J.M., 2001. Oxygen isotope variations of basaltic lavas and upper mantle rocks. Rev. Mineral. Geochem. 43, 319–364.

Eiler, J.M., Crawford, A., Elliott, T.I.M., Farley, K.A., Valley, J.W., Stolper, E.M., 2000. Oxygen isotope geochemistry of oceanic-arc lavas. J. Petrol. 41, 229–256.

Fisher, C.M., Vervoort, J.D., Hanchar, J.M., 2014. Guidelines for reporting zircon Hf isotopic data by LA-MC-ICPMS and potential pitfalls in the interpretation of these data. Chem. Geol. 363, 125–133.

Forsythe, R., Nelson, E., 1985. Geological manifestations of ridge collision: evidence from the Golfo de Penas-Taitao Basin, southern Chile. Tectonics 4, 477–495.

Forsythe, R.D., Nelson, E.P., Carr, M.J., Kaeding, M.E., Herve, M., Mpodozis, C., Soffia, J.M., Harambour, S., 1986. Pliocene near-trench magmatism in southern Chile: a possible manifestation of ridge collision. Geology 14, 23–27.

Gregory, R.T., Taylor, H.P., 1981. An Oxygen Isotope Profile in a section of cretaceous Oceanic Crust, Samail Ophiolite, Oman: evidence for $\delta^{18}O$ Buffering of the Oceans by deep (>5 km) Seawater-Hydrothermal Circulation at Mid-Ocean Ridges. J. Geophys. Res. 86, 2737–2755.

Guivel, C., Lagabrielle, Y., Bourgois, J., Maury, R.C., Fourcade, S., Martin, H., Arnaud, N., 1999. New geochemical constraints for the origin of ridge-subduction-related plutonic and volcanic suites from the Chile Triple Junction (Taitao Peninsula and Site 862, LEG ODP141 on the Taitao Ridge). Tectonophysics 311, 83–111.

Hervé, F., Fanning, M., Thomson, S.N., Pankhurst, R.J., Anma, R., Veloso, A., Herrera, C., 2003. SHRIMP U-Pb and FT Pliocene ages of near-trench granites in Taitao Peninsula, southern Chile. Simposium Sudamericano de Geología Isotópica. 4, pp. 190–193.

Hoskin, P.W.O., Ireland, T.R., 2000. Rare earth element chemistry of zircon and its use as a provenance indicator. Geology 28, 627–630.

Hoskin, P.W.O., Schaltegger, U., 2003. The composition of zircon and igneous and metamorphic petrogenesis. In: Hanchar, J.M., Hoskin, P.W.O. (Eds.), Zircon. Reviews in Mineralogy and Geochemistry. 53. Mineralogical Society of America, Washington, D. C, pp. 27–62.

Iizuka, T., Hirata, T., 2005. Improvements of precision and accuracy in in situ Hf isotope microanalysis of zircon using the laser ablation-MC-ICPMS technique. Chem. Geol. 220, 121–137.

Iizuka, T., Campbell, I.H., Allen, C.M., Gill, J.B., Maruyama, S., Makoka, F., 2013. Evolution of the African continental crust as recorded by U–Pb, Lu–Hf and O isotopes in detrital zircons from modern rivers. Geochim. Cosmochim. Acta 107, 96–120.

Iizuka, T., Yamaguchi, T., Hibiya, Y., Amelin, Y., 2015. Meteorite zircon constraints on the bulk Lu−Hf isotope composition and early differentiation of the Earth. Proc. Natl. Acad. Sci. 112, 5331–5336.

Iizuka, T., Yamaguchi, T., Itano, K., Hibiya, Y., Suzuki, K., 2017. What Hf isotopes in zircon tell us about crust–mantle evolution. Lithos 274, 304–327.

Ionov, D.A., Hofmann, A.W., Shimizu, N., 1994. Metasomatism-induced melting in mantle xenoliths from Mongolia. J. Petrol. 35, 753–785.

Ito, E., Clayton, R.N., 1983. Submarine metamorphism of gabbros from the Mid-Cayman rise: an oxygen isotopic study. Geochim. Cosmochim. Acta 47, 535–546.

Ito, E., Stern, R.J., Douthitt, C., 2003. Insights into operation of the subduction factory from the oxygen isotopic values of the southern Izu–Bonin–Mariana Arc. Island Arc 12, 383–397.

Iwamori, H., 2000. Thermal effects of ridge subduction and its implications for the origin of granitic batholith and paired metamorphic belts. Earth Planet. Sci. Lett. 181, 131–144.

Kaeding, M., Forsythe, R.D., Nelson, E.P., 1990. Geochemistry of the Taitao ophiolite and near-trench intrusions from the Chile margin Triple Junction. J. S. Am. Earth Sci. 3, 161–177.

Kay, R.W., 1978. Aleutian magnesian andesites: melts from subducted Pacific Ocean crust. J. Volcanol. Geotherm. Res. 4, 117–132.

Kay, R.W., Kay, S.M., 2002. Andean adakites: three ways to make them. Acta Petrol. Sin. 18, 303–311.

Kemp, A.I.S., Hawkesworth, C.J., Foster, G.L., Paterson, B.A., Woodhead, J.D., Hergt, J.M., Whitehouse, M.J., 2007. Magmatic and crustal differentiation history of granitic rocks from Hf-O isotopes in zircon. Science 315, 980–983.

Kempton, P.D., Hawkesworth, C.J., Fowler, M.B., 1991. Geochemistry and isotopic composition of gabbros from layer 3 of the Indian Ocean crust, Hole 735B. In: PT, Von Herzen R.E. Robinson, et al. (Eds.), Proceedings of the Ocean Drilling Program-Scientific Results. 118, pp. 127–141.

King, E.M., Valley, J.W., Davis, D.W., Edwards, G.R., 1998. Oxygen isotope ratios of Archean plutonic zircons from granite–greenstone belts of the Superior Province: indicator of magmatic source. Precambrian Res. 92, 365–387.

Kinoshita, O., 1999. A migration model of magmatism explaining a ridge subduction, and its details on a statistical analysis of the granite ages in cretaceous Southwest Japan. Island Arc 8, 181–189.

Kita, N.T., Ushikubo, T., Fu, B., Valley, J.W., 2009. High precision SIMS oxygen isotope analysis and the effect of sample topography. Chem. Geol. 264, 43–57.

Kon, Y., 2009. Origin of Ridge-Subduction Related Granitoids, Taitao Peninsula, Southern Chile. Ph.D. Thesis. Tokyo Institute of Technology.

Kon, Y., Komiya, T., Anma, R., Hirata, T., Shibuya, T., Yamamoto, S., Maruyama, S., 2013. Petrogenesis of the ridge subduction-related granitoids from the Taitao Peninsula, Chile Triple Junction Area. Geochem. J. 47, 167–183.

Lackey, J.S., Valley, J.W., Chen, J.H., Stockli, D.F., 2008. Dynamic Magma Systems, Crustal Recycling, and Alteration in the Central Sierra Nevada Batholith: the Oxygen Isotope Record. J. Petrol. 49, 1397–1426.

Lécuyer, C., Gruau, G., 1996. Oxygen and strontium isotope compositions of Hess deep gabbros (Holes 894F and 894G): High-temperature interaction of seawater with

the oceanic crust layer 3. Proceedings of the Ocean Drilling Program Scientific Results. 147, pp. 227–234.
Li, X.H., Li, W.X., Li, Q.L., Wang, X.C., Liu, Y., Yang, Y.H., 2010. Petrogenesis and tectonic significance of the~ 850 Ma Gangbian alkaline complex in South China: evidence from in situ zircon U–Pb dating, Hf–O isotopes and whole-rock geochemistry. Lithos 114, 1–15.
Martin, H., 1986. Effect of steeper Archaean geothermal gradient on geochemistry of subduction-zone magmas. Geology 14, 753–756.
Martin, H., 1999. Adakitic magmas: modern analogues of Archaean granitoids. Lithos 46, 411–429.
Martin, H., Moyen, J.F., Rapp, R., 2009. The sanukitoid series: magmatism at the Archaean–Proterozoic transition. Earth Environ. Sci. Trans. R. Soc. Edinb. 100, 15–33.
Matsuhisa, Y., 1979. Oxygen isotopic compositions of volcanic rocks from the arcs and their bearing on petrogenesis. J. Volcanol. Geotherm. Res. 5, 271–296.
Mattey, D., Lowry, D., Macpherson, C., 1994. Oxygen isotope composition of mantle peridotite. Earth Planet. Sci. Lett. 128, 231–241.
Mpodozis, C.M., Herve´, M., Nasi, C., Soffia, M.J., Forsythe, R.D., Nelson, E.P., 1985. El magmatismo plioceno de Peninsula Tres Montes y su relacion con la evolucion del punto triple de Chile austral: Revista Geológica de Chile. 25–26 pp. 13–28.
Nelson, E.P., Forsythe, R.D., 1989. Ridge collision at convergent margins: implications for Archean and post-Archean crustal growth. Tectonophysics 161, 307–315.
Nelson, E., Forsythe, R., Diemer, J., Allen, M., Urbina, O., 1993. Taitao Ophiolite: a ridge collision ophiolite in the forearc of southern Chile (46°S). Rev. Geol. Chile 20, 137–165.
Page, F.Z., Ushikubo, T., Kita, N.T., Riciputi, L.R., Valley, J.W., 2007a. High precision oxygen isotope analysis of picogram samples reveals 2-μm gradients and slow diffusion in zircon. Am. Mineral. 92, 1772–1775.
Page, F.Z., Fu, B., Kita, N.T., Fournelle, J., Spicuzza, M.J., Schulze, D.J., Viljoen, F., Basei, M.A.S., Valley, J.W., 2007b. Zircons from kimberlite: New insights from oxygen isotopes, trace elements, and Ti in zircon thermometry. Geochim. Cosmochim. Acta 71, 3887–3903.
Peacock, S.M., Rushmer, T., Thompson, A.B., 1994. Partial melting of subducting oceanic crust. Earth Planet. Sci. Lett. 121, 227–244.
Peck, W.H., Valley, J.W., Corriveau, L., Davidson, A., McLelland, J., Farber, D.A., 2004. Oxygen-isotope constraints on terrane boundaries and origin of 1.18-1.13 Ga granitoids in the southern Grenville Province. Memoirs-Geol. Soc. Am. 163–182.
Shibuya, T., Komiya, T., Anma, R., Ota, T., Omori, S., Kon, Y., Yamamoto, S., Maruyama, S., 2007. Progressive metamorphism of the Taitao ophiolite; evidence for axial and off-axis hydrothermal alterations. Lithos 98, 233–260.
Shin, K.C., Anma, R., Nakano, T., Orihashi, Y., Ike, S.I., 2015. The Taitao ophiolite-granite complex, Chile: Emplacement of ridge-trench intersection oceanic lithosphere on land and origin of calc-alkaline I-type granites. Episodes 38, 283–297.
Spicuzza, M.J., Valley, J.W., McConnell, V.S., 1998. Oxygen isotope analysis of whole rock via laser fluorination: an air-lock approach. Geol. Soc. Am. 30, 80 Abstracts with Programs.
Stakes, D.S., O'Neil, J.R., 1982. Mineralogy and stable isotope geochemistry of hydrothermally altered oceanic rocks. Earth Planet. Sci. Lett. 57, 285–304.
Stern, C.R., Kilian, R., 1996. Role of the subducted slab, mantle wedge and continental crust in the generation of adakites from the Andean Austral Volcanic Zone. Contrib. Mineral. Petrol. 123, 263–281.
Taylor Jr., H.P., Sheppard, S.M.F., 1986. Magmatic rocks: I. Processes of isotopic fractionation and isotope systematics. Stable isotopes in high temperature geological processes. Rev. Mineral. 16, 227–271.
Uyeda, S., Miyashiro, A., 1974. Plate tectonics and the Japanese Islands: a synthesis. Geol. Soc. Am. Bull. 85, 1159–1170.
Valley, J.W., 2003. Oxygen isotopes in zircon. Rev. Mineral. Geochem. 53, 343–385.
Valley, J.W., Kita, N.T., 2009. *In situ* Oxygen Isotope Geochemistry by Ion Microprobe. In: Fayek, M. (Ed.), MAC Short Course: Secondary Ion Mass Spectrometry in the Earth Sciences. 41, pp. 19–63.
Valley, J.W., Chiarenzelli, J.R., McLelland, J.M., 1994. Oxygen isotope geochemistry of zircon. Earth Planet. Sci. Lett. 126, 187–206.
Valley, J.W., Kitchen, N., Kohn, M.J., Niendorf, C.R., Spicuzza, M.J., 1995. UWG-2, a garnet standard for oxygen isotope ratios: strategies for high precision and accuracy with laser heating. Geochim. Cosmochim. Acta 59, 5223–5231.
Valley, J.W., Kinny, P.D., Schulze, D.J., Spicuzza, M.J., 1998. Zircon Megacrysts from Kimberlite: oxygen isotope variability among mantle melts. Contrib. Mineral. Petrol. 133, 1–11.
Valley, J.W., Lackey, J.S., Cavosie, A.J., Clechenko, C.C., Spicuzza, M.J., Basei, M.A.S., Bindeman, I.N., Ferreira, V.P., Sial, A.N., King, E.M., Peck, W.H., Sinha, A.K., Wei, C.S., 2005. 4.4 billion years of crustal maturation: Oxygen isotopes in magmatic zircon. Contrib. Mineral. Petrol. 150, 561–580.
Valley, J.W., Reinhard, D.A., Cavosie, A.J., Ushikubo, T., Lawrence, D.F., Larson, D.J., Kelly, T.F., Snoeyenbos, D., Strickland, A., 2015. Nano- and Micro-geochronology in Hadean and Archean Zircons by Atom-Probe Tomography and SIMS: New Tools for Old Minerals. Am. Mineral. 100, 1355–1377.
Van Kranendonk, M.J., Smithies, R.H., Griffin, W.L., Huston, D.L., Hickman, A.H., Champion, D.C., Anhaeusser, C.R., Pirajno, F., 2015. Making it thick: a volcanic plateau origin of Palaeoarchean continental lithosphere of the Pilbara and Kaapvaal cratons. Geol. Soc. Lond. Spec. Publ. 389, 83–111.
Veloso, E.A.E., Anma, R., Yamazaki, T., 2005. Tectonic rotations during the Chile Ridge collision and obduction of the Taitao Ophiolite (southern Chile). Island Arc 14, 599–615.
Wang, X.-L., Coble, M.A., Valley, J.W., Shu, X.-J., Kitajima, K., Spicuzza, M.J., Sun, T., 2014. Influence of radiation damage on late Jurassic zircon from southern China: evidence from in situ measurement of oxygen isotopes, laser Raman, U-Pb ages, and trace elements. Chem. Geol. 389, 122–136.